Ore Geology Reviews 86 (2017) 225–253

Contents lists available at ScienceDirect

Ore Geology Reviews

journal homepage: www.elsevier.com/locate/oregeo

Mechanism of mineralization in the Changjiang uranium ore field, South China: Evidence from fluid inclusions, hydrothermal alteration, and H–O isotopes

Chuang Zhang [a,b,*], Yuqi Cai [a,b], Hao Xu [a,b], Qian Dong [a,c], Jialin Liu [a,b], Ruixiang Hao [a,b]

[a] Beijing Research Institute of Uranium Geology, China National Nuclear Corporation, Beijing 100029, China
[b] Key Lab of Uranium Resource Prospecting and Evaluating Technology, China National Nuclear Corporation, Beijing 100029, China
[c] China University of Geoscience (Beijing), Beijing 100083, China

ARTICLE INFO

Article history:
Received 17 February 2016
Received in revised form 12 January 2017
Accepted 13 January 2017
Available online 29 January 2017

Keywords:
Mineralization mechanism
Changjiang uranium ore field
Fluid inclusion
Hydrothermal alteration
H–O isotopes

ABSTRACT

The Changjiang uranium ore field, which contains >10,000 tonnes of recoverable U with a grade of 0.1–0.5%, is hosted by Triassic two-mica and Jurassic biotite granites, and is one of the most important uranium ore fields in South China. The minerals associated with alteration and mineralization can be divided into two stages, namely syn-ore and post-ore. The syn-ore minerals are primarily quartz, pitchblende, hematite, hydromica, chlorite, fluorite, and pyrite; the post-ore minerals include quartz, calcite, fluorite, pyrite, and hematite. The fluid inclusions of the early syn-ore stage characteristically contain O_2, and those of the late syn-ore and post-ore stage contain H_2 and CH_4. The fluid inclusions in quartz of the syn-ore stage include H_2O, H_2O–CO_2, and CO_2 types, and they occur in clusters or along trails. Homogenization temperatures (T_h) for the H_2O–CO_2 and two-phase H_2O inclusions range from 106 °C to >350 °C and cluster in two distinct groups for each type; salinities are lower than 10 wt% NaCl equiv. The ore-forming fluids underwent CO_2 effervescence or phase separation at ~250 °C under a pressure of 1000–1100 bar. The U/Th values of the altered granites are lowest close to the ore, increase outwards, but subsequently decrease close to unaltered granites. From the unaltered granites to the ore, the lowest Fe_2O_3/FeO values become lower and the highest values higher. The REE patterns of the altered granites and the ores are similar to each other. The U contents of the ores show a positive correlation with total REE contents but a negative correlation with LREE/HREE ratios, indicating the pitchblende is REE-bearing and selectively HREE-rich. The δEu values of the ore show a positive correlation with U contents, indicating the early syn-ore fluids were oxidizing. The δCe values show a negative correlation, indicating the later mineralization environment became reducing. The water–rock interactions of the early syn-ore stage resulted in oxidization of altered granites and reduction of the ore-forming fluids, and it was this reduction that led to the uranium mineralization. During alteration in the early syn-ore stage, the oxidizing fluids leached uranium from granites close to faults, and Fe_2O_3/FeO ratios increased in the alteration zones. The late syn-ore and post-ore alteration decreased the Fe_2O_3/FeO ratios in the alteration zones. The $\delta^{18}O_{W\text{-}SMOW}$ values of the ore-forming fluids range from −1.8‰ to 5.4‰, and the $\delta D_{W\text{-}SMOW}$ values range from −104.4‰ to −51.6‰, suggesting meteoric water. The meteoric water underwent at least two stages of water–rock interaction: the first caused the fluids to become uranium-bearing, and the second stage, which was primarily associated with ore-bearing faults, led to uranium deposition as pitchblende, accompanied by CO_2 effervescence.

1. Introduction

The Changjiang uranium ore field is located in the Zhuguang granite massif, which straddles the boundaries between the provinces of Guangdong, Jiangxi, and Hunan in South China (Fig. 1) (Dahlkamp, 2009). This field was discovered in the late 1950s and has been mined for decades. Ores at Changjiang are characterized as low to medium grade (0.1–0.5% of U) and are positioned at shallow depths (some orebodies are close to the surface), which makes the ores profitable. The pre-mining resource is estimated to have exceeded 10,000 tonnes of recoverable uranium.

* Corresponding author at: No. 10 Xiaoguandongli, Beijing 100029, China.
E-mail address: zhangc198506@126.com (C. Zhang).

http://dx.doi.org/10.1016/j.oregeorev.2017.01.013
0169-1368/

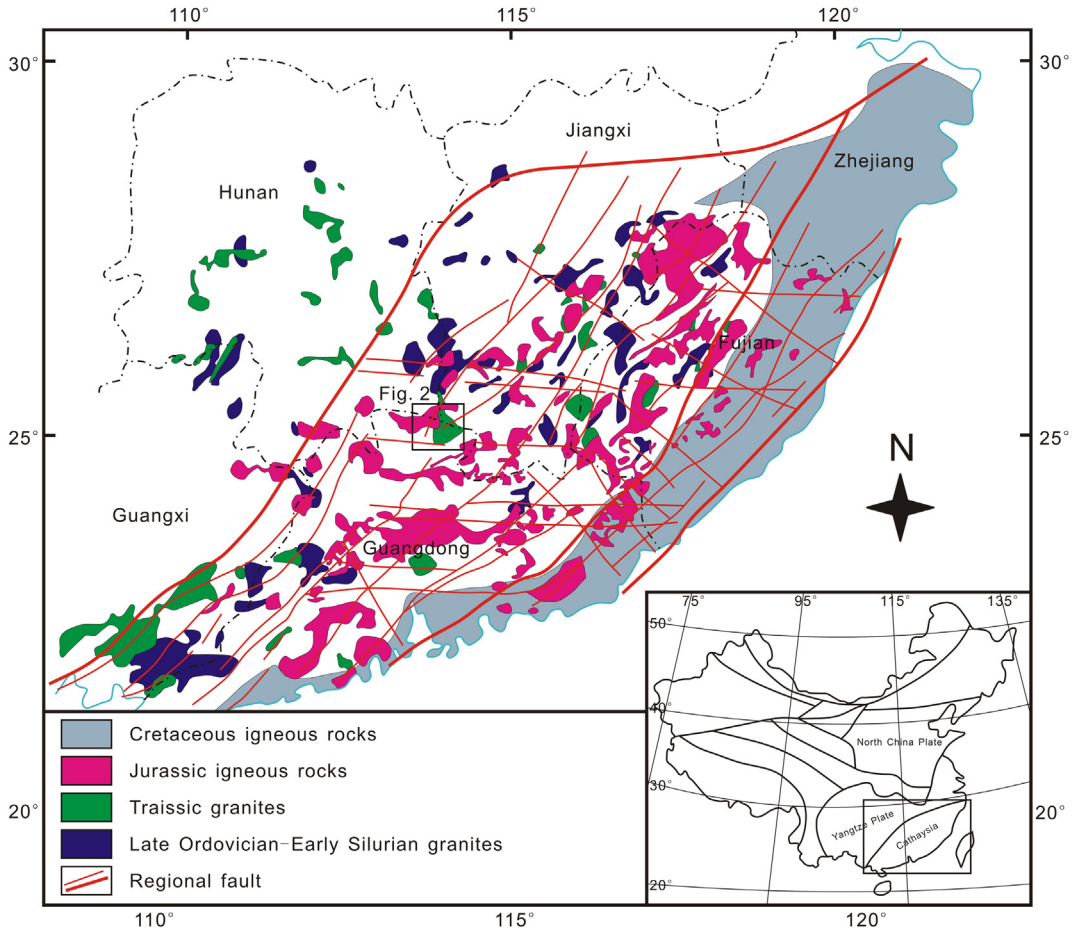

Fig. 1. Schematic map of the Cathaysia block showing the geological background and location of the Zhuguang granite massif (modified from Li et al., 2012; Wang et al., 2013a,b).

The Changjiang uranium ore field is hosted by medium-grained granites that formed in the Triassic and Jurassic (Wang et al., 2005; Sun, 2006; Li et al., 2010, 2012) (Fig. 2). In Cathaysia, there are many uranium deposits that occur in granites or volcanic rocks, such as the Sanerer (Min et al., 1999), Xiangshan, and Xiwang ore fields (Dahlkamp, 2009). Late Permian–Triassic and Jurassic granites, and NE–SW-trending fault zones are well developed throughout Cathaysia, whereas Cretaceous volcanic rocks are mainly restricted to southeastern Cathaysia (Fig. 1).

A number of Chinese publications have documented the uranium deposits that occur in the Zhuguang granite massif (i.e., Chen and Liu, 1990; Deng et al., 2003; Guo et al., 2010); however, the origin of the deposits remains debated.

Around the study area, there are metamorphic basement rocks, granites, and sedimentary basins, all of which are characterized by high uranium contents. Some researchers have suggested that these rocks were the main sources of uranium mineralization, particularly Triassic granites (Fig. 2) (Chen et al., 2007), based on rare earth element and Pb isotopic studies (Du, 1982; Zhang, 1994; Zhang et al., 2003; Min et al., 1999). According to Hu et al. (2004, 2007), the uranium mineralization, which occurred later than the formation of regional basins and mafic dikes, was a product of regional extension. Based on H–O isotopic studies, some geologists have proposed that the ore-forming fluids were a mixture of magmatic and meteoric water (Du and Wang, 1984; Hu et al., 1993; Min et al., 1999, 2005), whereas others have argued that the metallogenic material and ore-forming fluids were derived from the mantle (Deng et al., 2003; Jiang et al., 2004; Zhu et al., 2006; Wang and Li, 2007), though this has been refuted by the fact that mineralization occurred tens of million years later than the emplacement of the granites. Many geologists now believe that the uranium was sourced from the granites (Zhang, 2008), that the ore-forming fluids were meteoric water that experienced intense fluid–rock interactions with the granite (Hu et al., 1993), and that most of the uranium was transported in the ore-forming fluids as a complex of uranyl with CO_2 (Zhang, 2008). We note that the above-mentioned theories are inconsistent with each other, and that most previous studies have focused on isotope geochemistry rather than field data. In this paper, we present new data and observations that allow us to interpret the geological facts more reasonably and to test the earlier ideas. We propose a new model of U mineralization at Changjiang based on mineral paragenesis, fluid inclusion, geochemistry, and H–O isotope studies.

2. Regional geology

In the Zhuguang area, the metamorphic basement rocks are unconformably overlain by Cretaceous–Paleogene sedimentary rocks that were deposited in basins (Fig. 2). The metamorphic basement is more than 20 km thick (Zhang et al., 2005; Zhang, 2008) and composed mainly of metamorphosed marine sedimentary rocks of Sinian, Cambrian, Ordovician, Devonian, and Carboniferous age; Silurian rocks are absent. The Sinian, Cambrian,

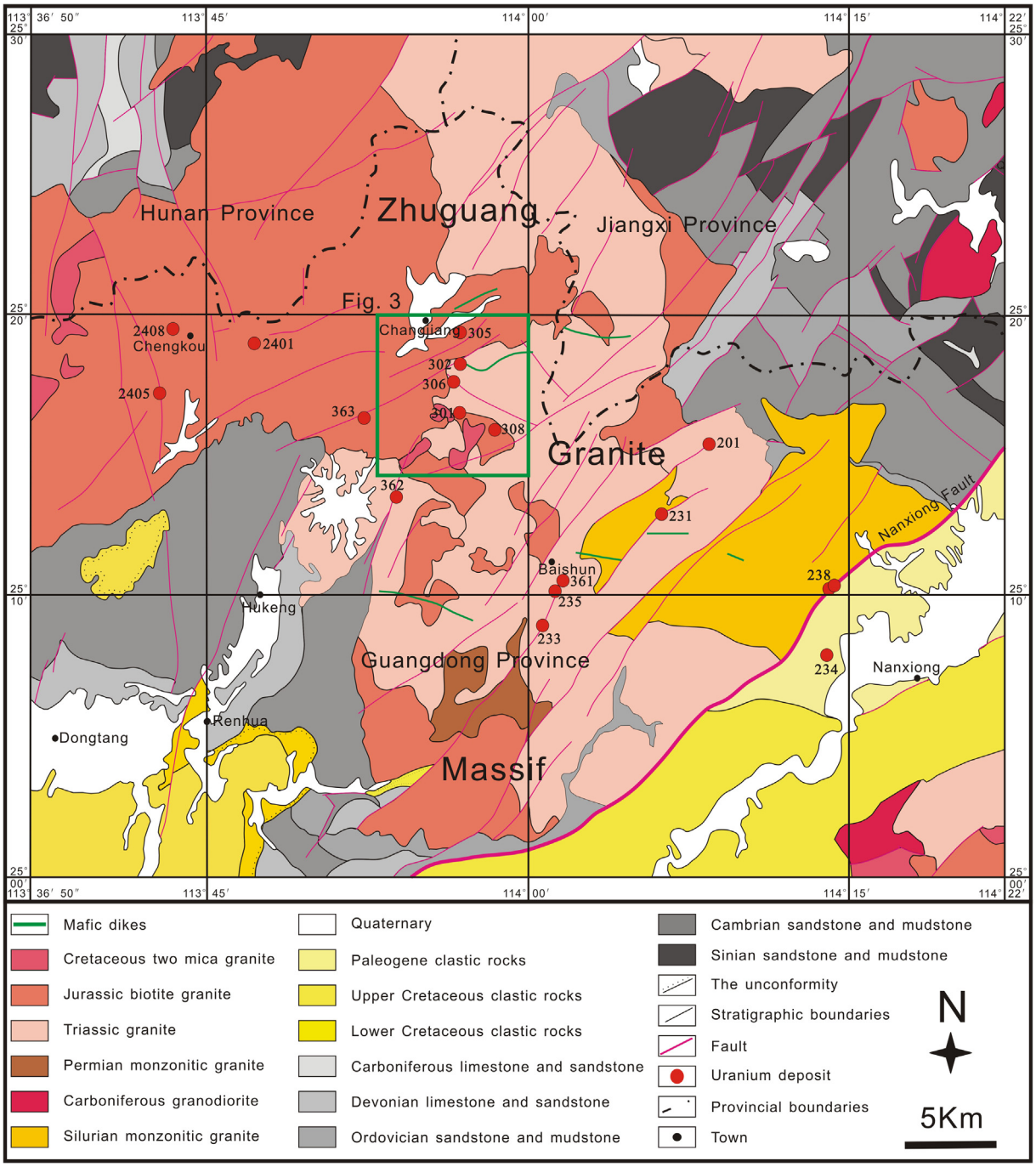

Fig. 2. Geological map of the Zhuguang granite massif showing that uranium deposits occur in granites and that Cretaceous-Paleogene basins are located to the south (modified from Zhang, 2008).

and Ordovician rocks are characterized by sandstones, mudstones, and limestones that underwent metamorphism and transformation to slates or phyllites with uranium contents of 4–10 ppm. The Devonian and Carboniferous rocks are characterized by limestones and sandstones with uranium contents of 2–4 ppm (Zhang, 2008).

The Cretaceous–Paleogene sedimentary rocks are located in the southern part of the Zhuguang granite massif (Fig. 2), and are composed of clastic rocks and molasse formations that formed in lacustrine or intermontane basins of Cretaceous, and Paleogene age. Their uranium contents are generally 6–10 ppm but locally reach 15 ppm (Zhang, 2008).

In the study area, the structures consist mainly of NE–SW, NW–SE, ~N–S, and E–W striking faults (Figs. 2 and 3), and in the Changjiang uranium ore field the ~N–S striking faults are the main ore-bearing structures. In addition to the ore-bearing faults, there are three NE–SW striking regional faults (Lizhou, Mianhuakeng, and Huangxishui faults, from north to south; Fig. 3), and one NW–SE striking Fault (Youdong fault).

The uranium orebodies are hosted by the Zhuguang granite massif (Fig. 3). The Zhuguang granite massif formed over a long period from the Silurian to the Cretaceous, and is exposed over an area of >4000 km^2. The granites in the Zhuguang massif are mainly peraluminous, with lithologies including two-mica granite,

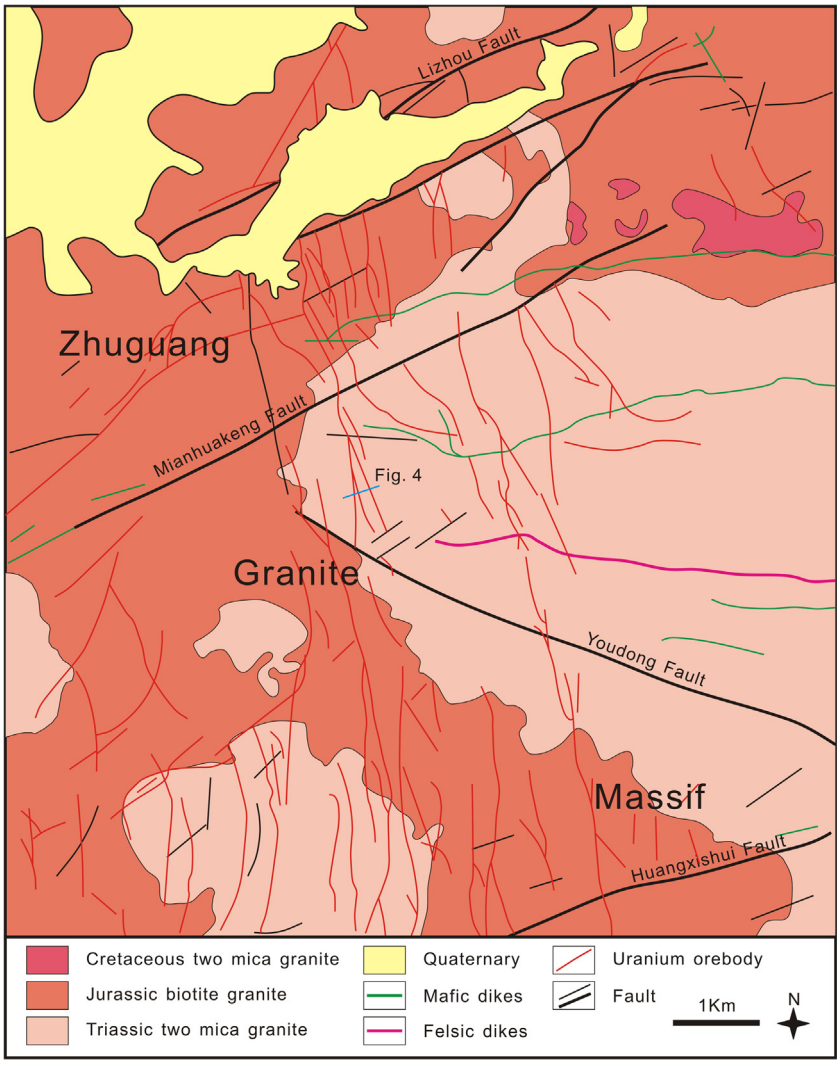

Fig. 3. Geological map of the Changjiang uranium ore field showing the location of Fig. 4; the nearly N-S striking faults are ore-bearing structures (Zhang, 2008).

biotite granite, monzonitic granite, and granodiorite. The minerals are commonly K-feldspar, plagioclase, biotite, and quartz, with accessory uraninite. The SiO_2 contents are typically 70–75 wt%, with $Na_2O + K_2O$ contents between 7 and 9 wt% (for details, see Dahlkamp, 2009). The uranium contents of the granitic rocks are generally 7–20 ppm (Zhang et al., 2005; Dahlkamp, 2009). Apart from the granitic rocks, there are mafic dikes that were emplaced along E–W, NE–SW, and ~N–S striking faults.

3. Mineralization and alteration

The mineralization is concentrated mainly along and adjacent to the N–S striking faults, and the orebodies are characteristically hundreds of meters long and several meters thick, with U grades of 0.1%–0.5%. The total reserves exceed 10,000 tonnes of recoverable uranium. The ores commonly occur as veins or lenses of quartz–pitchblende and in brecciated and altered granite. Using an isochron age deduced from the U–Pb dating of pitchblende, previous researchers have suggested that the mineralization occurred at 54–81 Ma, corresponding to the age of formation of the Cretaceous–Paleogene sedimentary basins to the south (Ludwig et al., 1985; Zhang, 2008; Huang et al., 2010).

The alteration around the uranium orebodies can be divided into outer, middle, and inner alteration zones, according to the alteration intensity and distance from the ores (Fig. 4). The inner alteration zones are within 20 m of the uranium ores (Fig. 4), and in these inner alteration zones the granites underwent advanced hydromica (illite) and chloritic alteration. At distances of 20–50 m from the ore-bearing faults, there is a middle zone characterized by moderate hydromica (illite) and chloritic alteration. At distances of 50–100 m from the ore-bearing faults there is an outer zone where hydromica (illite) and chloritic alteration is weak. The products of hydrothermal alteration associated with the mineralization are fine-grained (Fig. 5) and include the replacement of the original K-feldspar and plagioclase by hydromica (illite) and quartz, and the original biotite by chlorite and hematite, with the hematite occurring in bands along the foliation of the chlorite (Fig. 5).

Because of the substantial alteration around the uranium orebodies, many studies (Wang and Liu, 1987; Lin, 1990; Zhang, 1994; Zhang et al., 2003; Min et al., 1999) have suggested that the uranium was sourced from the altered granites, but this idea is refuted by our most recent research (see details in Section 6.2 Geochemistry).

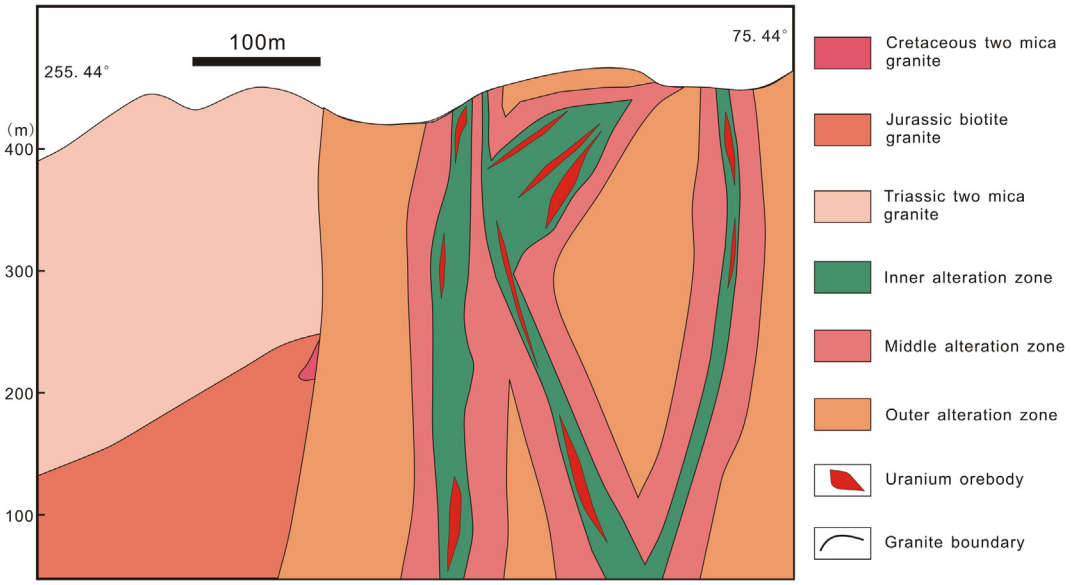

Fig. 4. A simplified cross-section of the Changjiang uranium ore field showing the distribution of alteration zones (modified from Zhang, 2008).

4. Mineral paragenesis

Thin section observations reveal that the minerals related to alteration and mineralization formed in three distinct stages: magmatic, syn-ore, and post-ore.

4.1. Magmatic stage

In the study area, the lithologies of the Zhuguang granite massif include two-mica granite, biotite granite, monzonitic granite, and granodiorite (Fig. 2). The two-mica granite is widespread in the south and east of the study area, and generally contains quartz (20%), K-feldspar (15%), plagioclase (35%), biotite (15%), and muscovite (10%), along with minor zircon and apatite; grain sizes vary from <0.2 to >5 mm. The biotite granite is characterized by porphyritic textures with K-feldspar phenocrysts. Its mineral composition is generally 25% quartz, 20% K-feldspar, 30% plagioclase, and 20% biotite, with minor amounts of muscovite; grain sizes vary from <0.2 to >5 mm. The monzonitic granite contains quartz (30%), K-feldspar (25%), plagioclase (30%), and biotite (10%), along with minor muscovite and other accessory minerals. The granodiorite generally contains quartz (15%), K-feldspar (15%), plagioclase (50%), and biotite (15%), along with minor muscovite and other accessory minerals. The main mineral species among these granites are the same, although their proportions vary, and these minerals form the basis for the hydrothermal alteration of the syn-ore stage.

4.2. Syn-ore stage

Around the uranium orebodies, the syn-ore hydrothermal fluids caused alteration of the magmatic minerals of the granitic rocks. The products of alteration include chlorite, hematite, hydromica (illite), and quartz (Fig. 5). The chlorite and hematite replaced biotite, while the hydromica (illite) and quartz replaced K-feldspar and plagioclase (Fig. 5). The abundance of hydromica increases with greater intensity of chloritic alteration. The chlorite is characteristically found as pseudomorphs of biotite, and contains bands of hematite along its foliations (Fig. 5). The hydromica (illite) is characteristically fine-grained, and together with quartz overprinted the K-feldspar and plagioclase. The alteration process can be expressed as follows:

$$\text{Plagioclase} + H_2O + K^+ + H^+ \rightarrow \text{Sericite} + \text{Quartz} + Na^+ + Ca^{2+}$$

$$NaAlSi_3O_8 + H_2O + K^+ + H^+ \rightarrow KAl_3Si_3O_{10}(OH)_2 + SiO_2 + Na^+$$

$$CaAl_2Si_2O_8 + H_2O + K^+ + H^+ \rightarrow KAl_3Si_3O_{10}(OH)_2 + SiO_2 + Ca^{2+}$$

$$\text{Plagioclase} + H_2O + K^+ + H^+ \rightarrow \text{Hydromica(illite)} + \text{Quartz} + Na^+ + Ca^{2+}$$

$$NaAlSi_3O_8 + H_2O + K^+ + H^+ \rightarrow K_{1-x}(H_2O)_x\{Al_2[AlSi_3O_{10}](OH)_{2-x}(H_2O)_x\} + SiO_2 + Na^+$$

$$CaAl_2Si_2O_8 + H_2O + K^+ + H^+ \rightarrow K_{1-x}(H_2O)_xAl_2\{[AlSi_3O_{10}](OH)_{2-x}(H_2O)_x\} + SiO_2 + Ca^{2+}$$

$$\text{K-feldspar} + H_2O + H^+ \rightarrow \text{Sericite} + \text{Quartz} + K^+$$

$$KAlSi_3O_8 + H_2O + H^+ \rightarrow KAl_3Si_3O_{10}(OH)_2 + SiO_2 + K^+$$

$$\text{K-feldspar} + H_2O + H^+ \rightarrow \text{Hydromica(illite)} + \text{Quartz} + K^+$$

$$KAlSi_3O_8 + H_2O + H^+ \rightarrow K_{1-x}(H_2O)_x\{Al_2[AlSi_3O_{10}](OH)_{2-x}(H_2O)_x\} + SiO_2 + K^+$$

$$\text{Biotite} + O_2\text{(Details in fluid inclusions)} \rightarrow \text{Chlorite} + \text{Hematite}$$

$$K\{(Mg_{<0.67}, Fe_{>0.33})_3[AlSi_3O_{10}](OH)_2\} + O_2 \rightarrow (Mg, Fe)_{5-6}[(Al, Si)_4O_{10}](OH)_8 + Fe_2O_3 + K^+$$

Corresponding to the alteration, there are veins that contain quartz, pitchblende, and pyrite in fractures. The quartz and pyrite grains are usually euhedral or subhedral, with sizes of <10 to >100 μm, and the pitchblende is made up of aggregates of small uraninite (UO_{2+x}, x < 1) grains. The pitchblende veins contain small

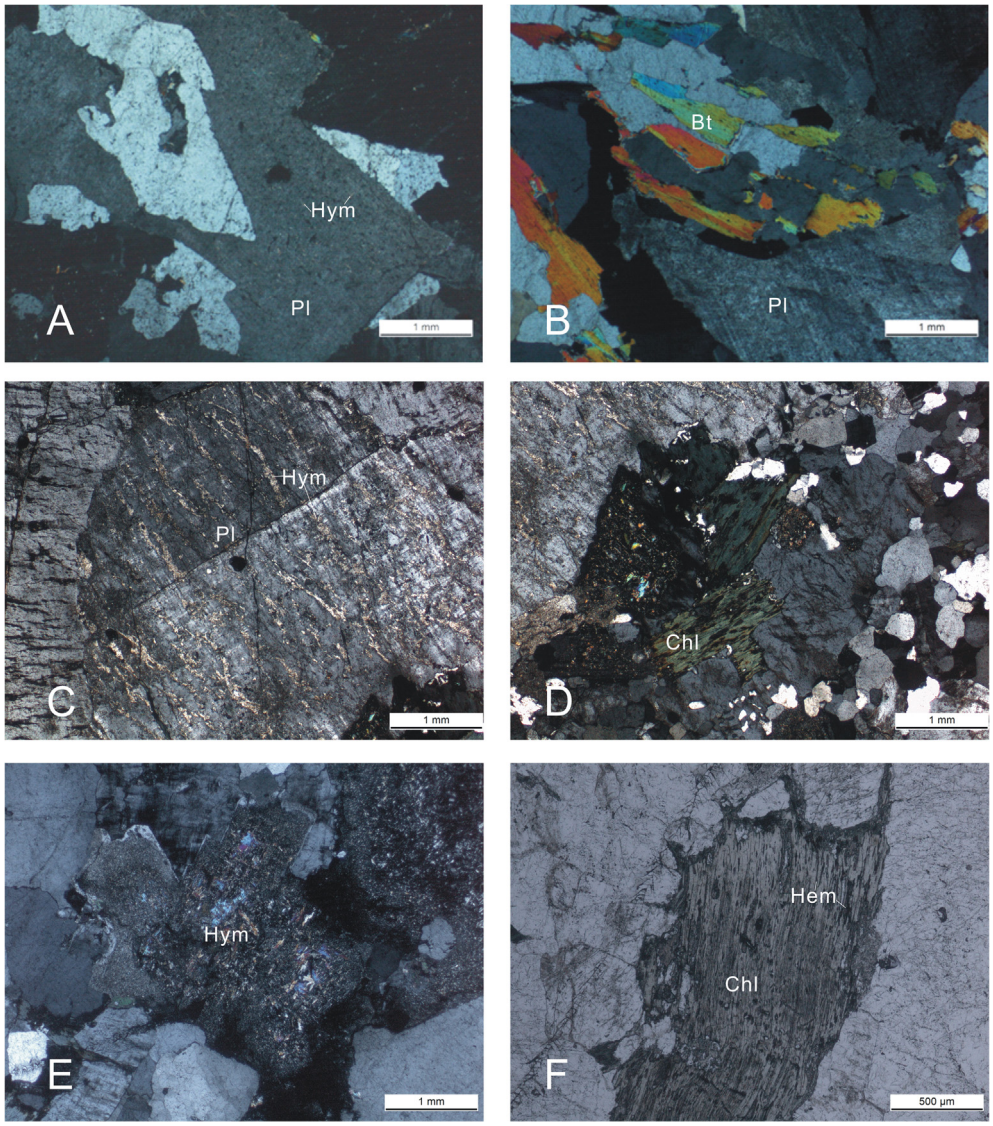

Fig. 5. Photomicrographs of altered granites from the Changjiang uranium ore field. A. Dotted hydromica alteration overprinted on the plagioclase of Jurassic biotite granite (Sample ZK3-2 170 m, cross-polarized light, outer alteration zone). B. Sparse part of biotite was converted to chlorite (Sample ZK3-2 170 m, cross-polarized light, outer alteration zone). C. Banded hydromica alteration overprinted on the microcline of monzonitic granite (Sample ZK9-1 100 m, cross-polarized light, intermediate alteration zone). D. Large part of biotite converted to chlorite with some hematite occurring in the foliations (Sample ZK9-1 100 m, cross-polarized light, intermediate alteration zone). E. Whole plagioclase altered into fine-grained hydromica and quartz (Sample ZK16-2 197 m, cross-polarized light, inner alteration zone). F. Whole biotite converted to chlorite with hematite occurring in the foliations (Sample ZK16-2 197 m, plain-transmitted light, inner alteration zone). Hym: hydromica, Bt: biotite, Pl: plagioclase, Hem: hematite, Chl: chlorite.

pyrite grains, indicating an association between pyritization and the uranium mineralization (Fig. 6A, D, F, and G). Associated with the pitchblende veins is a pervasive hematitization, which makes the thin sections red (Fig. 6B, C).

4.3. Post-ore stage

The pitchblende veins are cut by fluorite and hematite veins, indicating that fluorite and hematite formed later than the uranium mineralization (Fig. 6A, B, D, and E). In the fluorite veins, that the quartz grains grew on the crystal surfaces of the fluorite, which suggests that the quartz formed later than the fluorite (Fig. 6H and I). The quartz and fluorite grains are usually euhedral or subhedral, with sizes up to 1 mm. The hematite veins are made up of aggregates of small grains. Based on the above observations, we summarize the mineral paragenesis in Fig. 7.

5. Samples and analytical methods

Sixty-four samples were selected from drill cores and mining tunnels at the Changjiang uranium ore field, including ores and altered granites. The thin sections were examined using a DM2500P (LEICA Microsystems) microscope with transmitted light to determine the types and occurrence of fluid inclusions. The microthermometric measurements of the fluid inclusions and the laser Raman experiments were conducted on doubly polished thin sections using a Linkam TH600 heating–cooling stage and a LABHR–VIS LabRAM HR800 Raman microscope, respectively, using standard techniques (Shepherd et al., 1985) at the Geological Analysis and Testing Center, Beijing Research Institute of Uranium Geology, Beijing, China.

In the context of the mineral paragenetic sequence and our studies of the fluid inclusions, we then conducted studies of H iso-

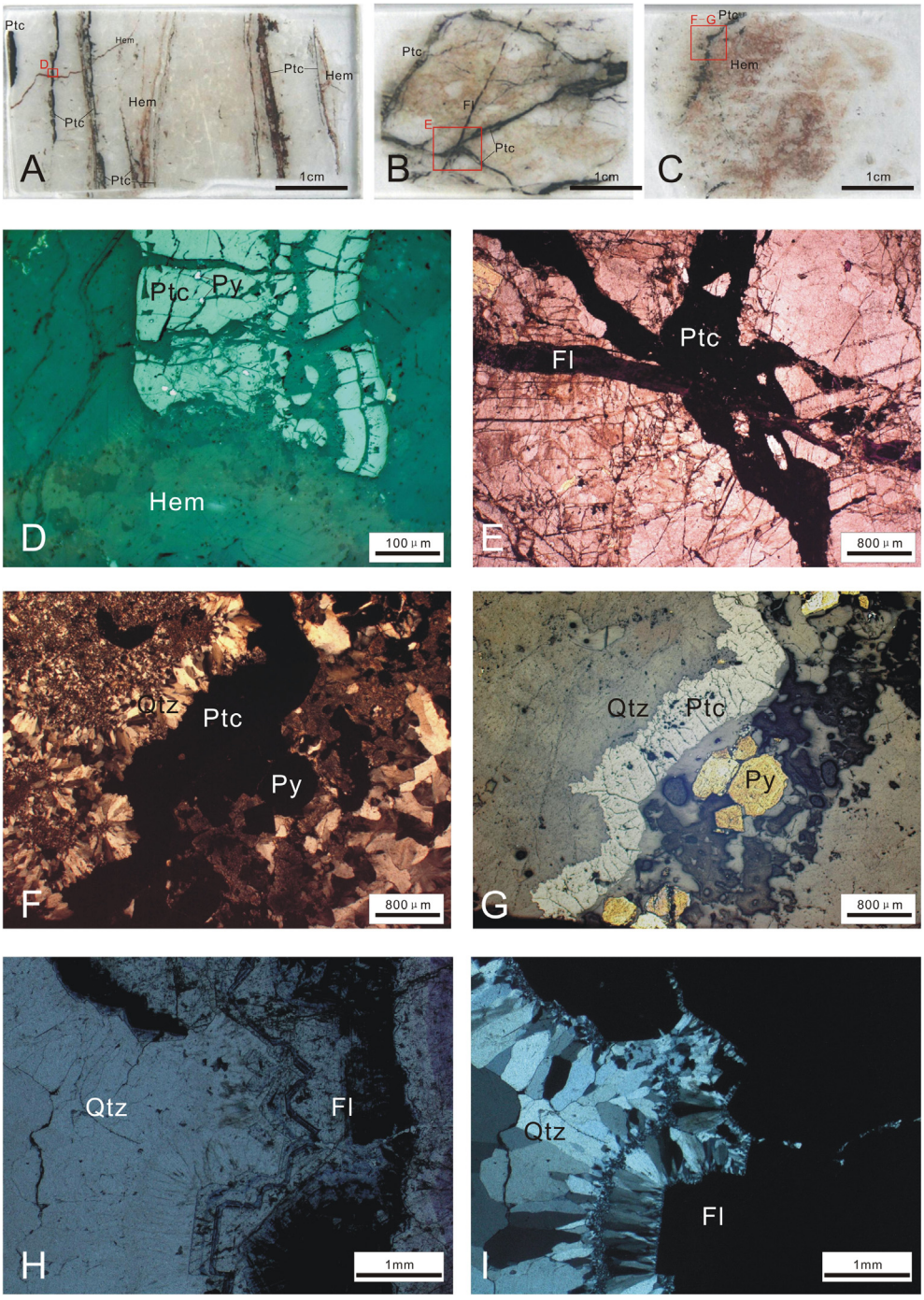

Fig. 6. Photographs of uranium mineralization from the Changjiang uranium ore field. A. Ore thin section with hematite matrix featuring parallel pitchblende veins cut through by hematite veins (Sample MHK-BP-05). B. Ore thin section with hematite matrix featuring rhombus pitchblende veins cross-cut by fluorite veins (Sample MHK-BP-04). C. Ore thin section with hematite matrix and pitchblende veins (Sample MHK-BP-09). D. Pyrite grains containing pitchblende veins cross-cut by hematite veins (Reflected light). E. Rhombus pitchblende veins cut through by fluorite veins (Plain-transmitted light). F. Pitchblende vein associated with quartz (Cross-polarized light). G. Pyrite associated with pitchblende veins (Reflected light). H & I. Quartz grains crystallized on the surface of fluorite in a quartz-fluorite vein (Sample SLQ-ZK18-2, H: Parallel transmitted light, I: cross-polarized light). Ptc: pitchblende, Fl: fluorite, Py: pyrite, Hem: hematite, Qtz: quartz.

topes in the fluid inclusions of the quartz–pitchblende veins and O isotopes in the quartz. Before any of this H–O isotopic work was done, the post-ore veins and surrounding rocks were removed, and the quartz–pitchblende veins were washed with distilled water, dried naturally, and subsequently crushed for analysis. Quartz grains were selected manually from a 20–40 mesh distribution under a binocular stereo-microscope, and the purity was better than 99%. The oxygen isotope compositions of the quartz were measured using the BrF_5 method of Clayton and Mayeda (1963), and the hydrogen isotope compositions of the quartz-hosted fluid inclusions were determined using the methods of Kyser and O'Neil (1984). The H–O isotope compositions were measured using a Finnigan MAT 253 mass spectrometer, and are reported in δ notation in units of per mil relative to the standard VSMOW. Replicate $\delta^{18}O$

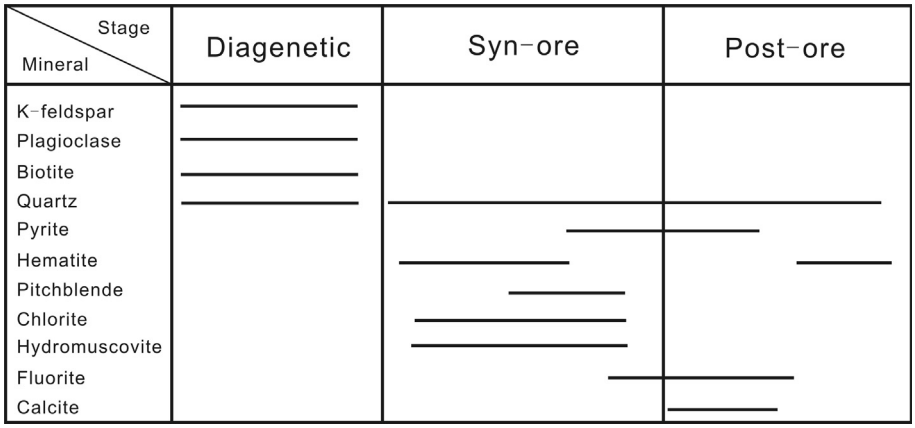

Fig. 7. Paragenetic sequences for the Changjiang uranium ore field, including magmatic, syn-ore and post-ore stage.

analyses were reproducible to ±0.2‰ and δD values to ±3‰. Oxygen isotope fractionation factors used throughout this paper are those suggested by Clayton et al. (1972) for water–quartz. Stable isotope measurements were performed at the Geological Analysis and Testing Center, Beijing Research Institute of Uranium Geology.

After petrographic examination, ore samples with no alteration and with weak, moderate, and intensive alteration were selected for geochemical analysis. Major element oxides were analyzed using a PHILIPS PW2404 X-ray fluorescence spectrometer, and trace elements were analyzed using a Finnigan MATHR–ICP–MS (Element I) at the Geological Analysis and Testing Center, Beijing Research Institute of Uranium Geology. The calibration lines used for quantification were produced by bivariate regression of data obtained from 36 reference materials encompassing a wide range of silicate compositions (Li et al., 2005), and analytical uncertainties ranged between 1% and 5%. A set of USGS and Chinese national rock standards, including BHVO-1, W-2, AGV-1, G-2, GSR-1, and GSR-3, was used for calibrating element concentrations of unknowns, and the analytical precision was typically 2–5%.

6. Results

6.1. Fluid inclusions

The fluid inclusion research was conducted firstly with optical microscopy observation which is the base of later microthermometry and Laser Raman Analysis. This work indicated that the types of fluid inclusions in syn-ore and post-ore minerals are similar to each other.

6.1.1. Occurrences and types

The primary fluid inclusions in vein samples occur in clusters or along trails that do not cut through grain boundaries (Figs. 8A, C, 9A), while in altered granites the fluid inclusions form numerous trails, most of which cut across grain boundaries. It is difficult to determine their relative ages, although many secondary trails intersect each other. Accordingly, we infer that most of the inclusions along secondary trails were trapped more or less contemporaneously, either during or shortly after the syn-ore stage (Fig. 8B, D, B). Based on the preliminary optical microscopy observations, three types of fluid inclusion, the H_2O, H_2O–CO_2, and CO_2 types, were identified in a single cluster or trail, indicating they were trapped contemporaneously during the syn-ore stage, as showing in Fig. 8A, B, C, and D. Inclusions that underwent post-entrapment changes (i.e., necking down, sharp corners) were locally observed in the selected samples using conventional microscopy, but only fluid inclusions without these textures were selected for this study. The sizes of CO_2 inclusions typically vary from <3 to >10 μm, even within one cluster, and they have oval, irregular, or negative crystal shapes. Most of the H_2O–CO_2 inclusions consist of three phases (liquid H_2O, liquid CO_2, and vapor CO_2) but have different amounts of CO_2 fill (from 10% to 90%, even within one cluster; Fig. 8C). These inclusions generally have oval, irregular, or negative crystal shapes, with sizes varying from <3 to >15 μm. The H_2O inclusions typically measure <10 μm, and commonly have a bubble fill (vapor H_2O) that is less than 20%; they generally have oval, irregular, or negative crystal shapes.

The post-ore stage quartz, calcite, and fluorite contain fluid inclusions useful for inclusion research. In the calcite grains, inclusions consist primarily of H_2O (Fig. 8E, one phase), CO_2, and H_2O–CO_2 types, all of which typically measure <15 μm, have oval, irregular, or parallelogram shapes, and occur in trails that do not cut across grain boundaries (Fig. 9C). The inclusions in fluorite are mainly CO_2 and H_2O–CO_2 types (Fig. 8F), and they occur mainly in three-dimensional clusters, but with a few in trails (Fig. 9D). These inclusions are usually oval, irregular, or triangular in shape, with diameters generally <15 μm.

6.1.2. Microthermometry

For the microthermometry, we focused on the syn-ore stage, and selected nine samples, which included altered granite and quartz–pitchblende veins. Samples 4-150-4, ZN14, ZN3, and ZN45-1 were collected from the inner alteration zone, and ZN10, 10029-1, 10029-14, 15029-1, and 15029-14 from quartz–pitchblende veins. In these samples, the inclusions are dominantly CO_2 and H_2O–CO_2 types with CO_2 contents of 20–80 vol%, and there are also small numbers of H_2O inclusions. Some fluorite and quartz–calcite veinlets cut through these samples. The quartz–pitchblende veins contain fewer inclusions than the altered granite samples, and these inclusions generally measure <5 μm, which make microthermometry difficult.

Table 1 summarizes the microthermometric characteristics of the fluid inclusions, and Table 2 summarizes the calculated pressure–temperature–compositional data. The full microthermometric and pressure–temperature–compositional data obtained during this study are reported in Appendices A and B, respectively. The CO_2 melting temperatures in CO_2 inclusions range from −61.0 to −57.4 °C, which are lower than −56.6 °C (i.e., the temperature of the triple point for pure CO_2), and the homogenization temperatures of CO_2 are concentrated between 17.8 and 22.1 °C. The CO_2 melting temperatures of H_2O–CO_2 inclusions range from −58.6 to −56.8 °C, which are slightly higher than those of the CO_2 inclu-

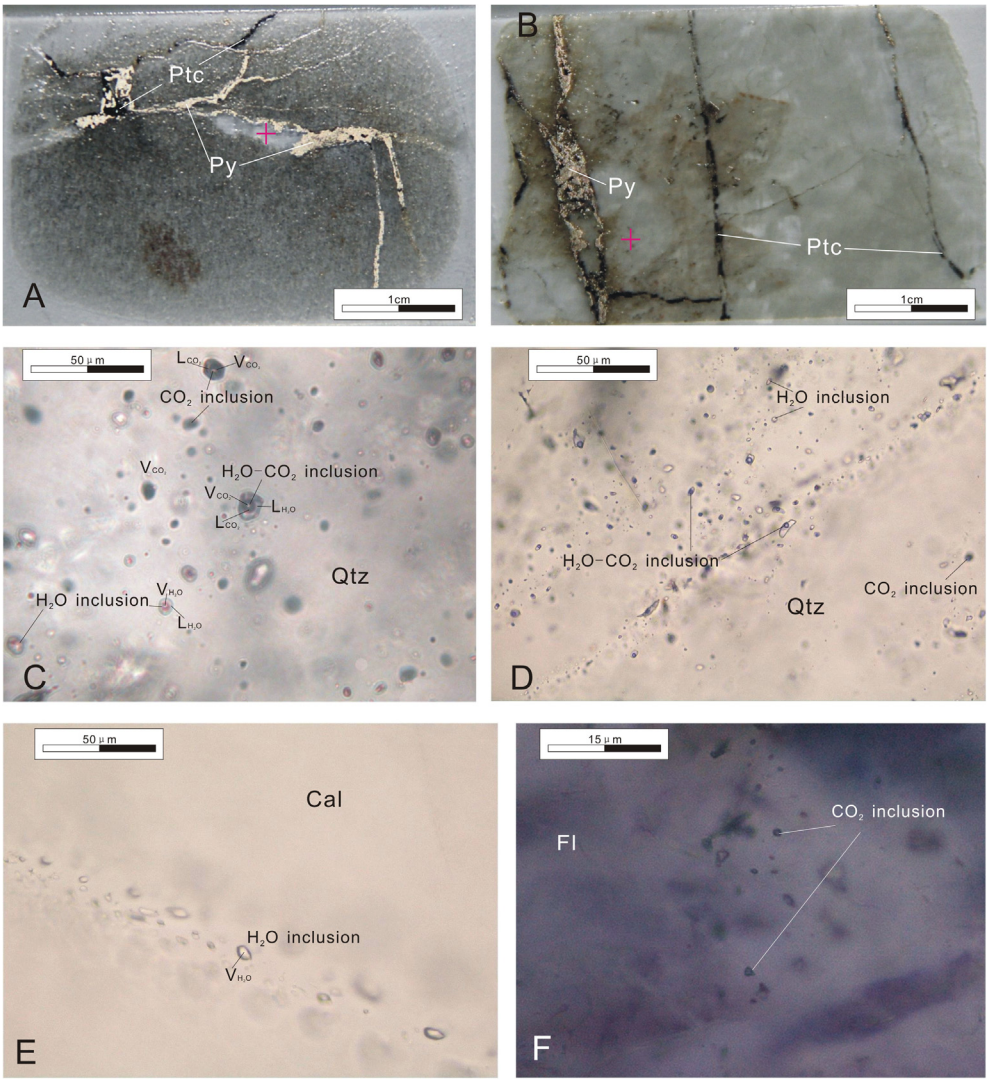

Fig. 8. Photomicrographs of fluid inclusions in the Changjiang uranium ore field. A. Overview of thin section of sample 10029–1, showing approximate location of Fig. 8C (red '+', wall rock is dark xenolith in granite), suggesting the fluid inclusions in Fig. 8C is syn-ore stage. B. Overview of thin section of sample 4–150-4, showing approximate location of Fig. 8D (red '+', wall rock is granite), and suggesting the fluid inclusions in Fig. 8D is probably syn-ore stage. C. Primary fluid inclusions occurring in clusters in quartz grain of the quartz-pitchblende-pyrite veins, showing that the syn-ore fluid inclusion assemblage includes H_2O-type, H_2O-CO_2-type, and CO_2-type (Sample 10029–1, syn-ore stage). D. Fluid inclusions clusters and along trails in quartz grain of the altered granites, showing the syn-ore fluid inclusion assemblage is containing H_2O-type, H_2O-CO_2-type, and CO_2-type (Sample 4–150-4, syn-ore stage). E. Primary fluid inclusions trails in calcite grain of the quartz-calcite veins (Sample 4–150-6, post-ore stage). F. Primary fluid inclusions cluster in fluorite grain of the fluorite veins (Sample CJ-QY-17, post-ore stage). (For interpretation of the references to colour in this figure legend, the reader is referred to the web version of this article.)

sions. In the H_2O–CO_2 inclusions, the clathrate disappearance temperatures range from 4.9 to 8.1 °C, the CO_2 homogenization temperatures range from 24.5 to 30.0 °C (higher than for the CO_2 inclusions), and the total homogenization temperatures range from 198 to 354 °C (Fig. 10). In contrast with the H_2O–CO_2 inclusions, the homogenization temperatures of H_2O inclusions are much lower and range from 106 to 254 °C (Fig. 10). The melting temperatures of ice are concentrated between −0.8 and −3.4 °C.

6.1.3. Laser Raman analysis

We used laser Raman analysis to examine syn-ore samples of inclusions in quartz–pitchblende veins and altered granites, and post-ore samples of inclusions in fluorite veins. The results suggest there are two types of fluid inclusion at the syn-ore stage according to gas composition: the first type characteristically contains O_2, and the second CH_4 and H_2 (Fig. 11). The fluid inclusions of the post-ore stage are mainly of the second type. In the syn-ore stage, the second type generally occurs much less frequently than the first type. It is difficult to determine the relative ages of the inclusions by microscopic observation and laser Raman analysis, but we infer that the second type occurs later than the first type in the syn-ore stage, and that a portion of the second type is probably composed of post-ore stage fluid inclusions (see details in Section 7, Discussion).

6.2. Geochemistry

6.2.1. U–th

There are two types of ore-hosting granite in the study area: two-mica granite and biotite granite. In the unaltered granites, the U and Th contents of these two types differ from each other. In the two-mica granites, the U contents are 135–162 ppm, the Th contents are 22.3–38.7 ppm, and U/Th ratios are 4.1–6.1, with an average of 4.8. In contrast, the biotite granites have lower U con-

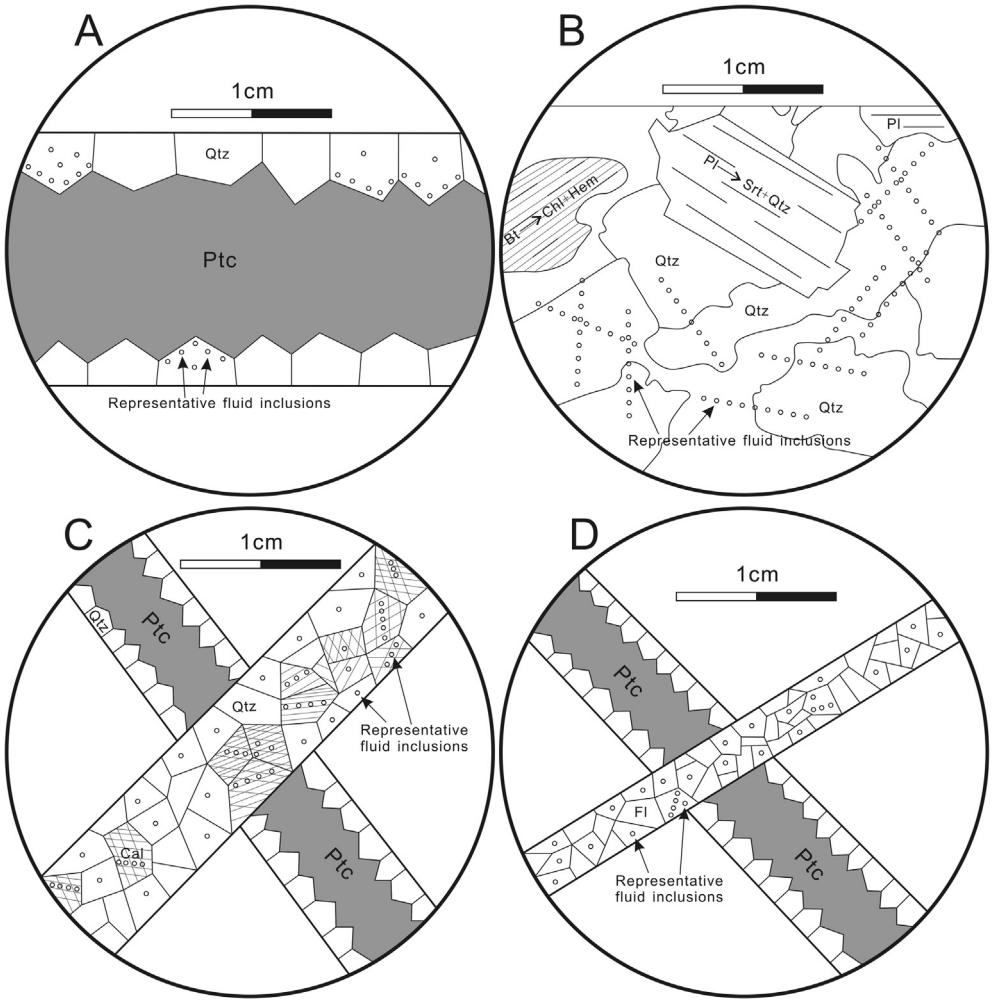

Fig. 9. Schematic diagrams showing the occurrence of fluid inclusions from the Changjiang uranium ore field. A. Schematic diagram of the occurrence of fluid inclusions in quartz-pitchblende veins, corresponding to Fig. 8 C. B. Schematic diagram of the occurrence of fluid inclusions in altered granites, corresponding to Fig. 8 D. C. Schematic diagram of the occurrence of fluid inclusions in quartz-calcite veins, corresponding to Fig. 8 E. D. Schematic diagram of the occurrence of fluid inclusions in fluorite veins, corresponding to Fig. 8 F.

tents (31.9–81.7 ppm), Th contents of 31.1–52.4 ppm, and U/Th ratios of 1.0–1.6 (average 1.4), which are much lower than in the two-mica granites (Fig. 12).

6.2.1.1. Altered two-mica granite. As shown in Fig. 12 and Appendix C, the U contents of samples from the outer, middle, and inner alteration zones, from close to ores and from the ores themselves are 265–323, 123–416, 54.8–209, 48.6–223, and 719–53,581 ppm, respectively; the corresponding Th contents are 47.7–52.2, 41.0–51.1, 24.8–54.9, 48.2–132, and 24.5–51.9 ppm, respectively, and the U/Th ratios are 5.5–6.2, 3.0–8.8, 1.6–6.8, 1.0–1.7, and 21.5–2187, respectively.

6.2.1.2. Altered biotite granite. For the biotite granite, the U contents of samples from the outer, middle, and inner alteration zones, from close to the quartz–pitchblende veins and from the quartz–pitchblende veins themselves are 37.1–100, 15.7–55.6, 155–528, 34.2–52.4, and usually >1000 ppm, respectively; the corresponding Th contents are 39.7–48.7, 9.8–45.7, 34.3–51, 45.8–72.3, and generally <50 ppm, respectively, and the U/Th ratios are 0.9–2.2, 1.0–1.7, 4.0–10.4, 0.7–0.8, and generally >20, respectively.

According to the mentioned above, the U/Th ratios are lowest in samples close to the ores. From the inner to the middle alteration zone, the U/Th ratios increase, and in the outer alteration zone the U/Th ratios are close to those of unaltered granite (Fig. 12).

6.2.2. Fe^{3+} & Fe^{2+}

6.2.2.1. Two-mica granite. The samples from unaltered two-mica granites, from the outer, middle, and inner alteration zones, and from adjacent to the ores and from the ores themselves that developed from the alteration of two-mica granite have Fe_2O_3/FeO values of 0.09–0.30, 0.19–0.32, 0.09–0.29, 0.14–1.4, 0.10–0.12, and 0.09–0.55, respectively (Fig. 13).

6.2.2.2. Biotite granite. Samples of biotite granite from the unaltered zone, the outer, middle, and inner alteration zones, adjacent to the quartz–pitchblende veins, and the quartz–pitchblende veins themselves have Fe_2O_3/FeO values of 0.19–0.39, 0.28–0.35, 0.14–0.25, 0.16–0.42, 0.08–0.27, and 0.01–2.25, respectively (Fig. 13).

6.2.3. REEs

The REE data for our samples are shown in Fig. 14. Although samples were taken from different alteration zones, the REE diagrams exhibit similar shapes, except for a few which show small positive δCe anomalies. Significantly, there are no appreciable differences between the altered biotite granite, the altered two-mica

Table 1
Summary of Fluid inclusion Microthermometry data from the Changjiang uranium ore field.

Stage	Sample No.	Fluid inclusion type	n	Fill	Tm(ice)	Tm(CO_2)	Tm(clathrate)	Th(CO_2)	Th(total)	Homogenize into L or V	Salinity (wt% NaCl equiv)
Syn-	4-150-4	CO_2	2	100	na	−61.0	na	17.8–19.2	na	L	0
		H_2O-CO_2	8	20–80	na	−57.0 to −58.6	6.6–7.5	28.6–30	198–353	L(V)	4.87–6.46
Syn-	ZN14	CO_2	2	100	na	−57.4 to −57.5	na	19.4–20	na	L	0
		H_2O-CO_2	9	20–90	na	−56.9 to −57.8	4.9–7.9	24.8–29.2	314–354	L(V)	4.14–9.24
Syn-	ZN3	CO_2	3	100	na	−57.6 to −57.9	na	19.2–22	na	L	0
		H_2O-CO_2	7	20–90	na	−56.8 to −58.0	6.4–8.1	26.8–27.9	264–317	L(V)	3.76–6.81
Syn-	ZN45-1	CO_2	3	100	na	−57.4 to −58.0	na	19.9–22.1	na	L	0
		H_2O-CO_2	12	20–80	na	−56.9 to −58.2	5.9–7.7	24.5–29.8	209–330	L(V)	4.51–7.64
		H_2O	11	10–15	−0.8 to −3.4	na	na	na	106–254	L	2.39–5.55
Syn-	ZN10	H_2O	3	10–15	−1.7 to −3.0	na	na	na	140–212	L	2.89–4.94
Syn-	15029-1	H_2O	4	15	−1.9 to −2.6	na	na	na	136–230	L	3.21–4.32
Syn-	15029-14	H_2O	2	5–10	−1.8 to −3.1	na	na	na	172–214	L	3.05–5.09
Syn-	10029-14	H_2O	7	5–10	−1.5 to −3.0	na	na	na	153–227	L	2.56–4.94
Syn-	10029-1	H_2O	4	15	−1.6 to −2.2	na	na	na	137–232	L	2.72–3.69

Syn-: fluid inclusion that captured in quartz of syn-ore stage; n: the number of tested fluid inclusions; For H_2O-CO_2 inclusion, fill is Vol% CO_2/(CO_2 + H_2O); for H_2O inclusion, fill is V/(V + L); Tm(ice): melting temperature of ice in H_2O fluid inclusion; Tm(CO_2): melting temperature of solid CO_2 phase in H_2O-CO_2 or CO_2 fluid inclusion; Tm(clathrate): melting temperature of clathrate in H_2O-CO_2 fluid inclusion; Th(CO_2): homogenization temperature of CO_2 phase in H_2O-CO_2 or CO_2 fluid inclusion; Th(Total): finial homogenization temperature of fluid inclusion.

Table 2
Summary of average calculated compositional and pressure data from the Changjiang uranium ore field.

Stage	Sample No.	Fluid inclusion type	n	Th	XH_2O	XCO_2	XNaCl	wt% NaCl equiv	Bulk density	Bulk molar vol	P-T isochors (P in bars; T in °C)				
											100	200	300	400	500
Syn-	4-150-4	CO_2	1	17.8	0	1	0	0	0.769	55.3	460.01	956.43	1432.9	1889.85	2331.28
		H_2O-CO_2	6	303	0.809	0.176	0.015	5.68	0.894	25.947	−1565.11	90.58	1517.76	2860.56	4115.54
Syn-	ZN14	CO_2	2	19.7	0	1	0	0	0.779	56.48	432.84	905.16	1359.08	1794.58	2215.32
		H_2O-CO_2	8	332	0.743	0.241	0.015	6.29	0.874	28.514	−1171.65	225.13	1434.79	2588.7	3665.67
Syn-	ZN3	CO_2	3	20.9	0	1	0	0	0.768	57.30	415.76	872.29	1311.42	1732.82	2139.99
		H_2O-CO_2	7	299	0.668	0.321	0.011	5.05	0.832	32.211	−870.98	297.95	1298.38	2243.57	3122.45
Syn-	ZN45-1	CO_2	3	20.8	0	1	0	0	0.769	57.23	417.48	875.63	1316.28	1739.13	2147.69
		H_2O-CO_2	10	292	0.804	0.179	0.016	6.12	0.904	25.819	−1494.47	161.25	1600.15	2962.89	4238.35
		H_2O	10	219	0.9883	0	0.0117	3.69	0.869	21.267	−1806.93	−272.39	1262.14	2796.67	4331.2
Syn-	ZN10	H_2O	3	187	0.9873	0	0.0127	4.01	0.911	20.432	−1490.98	233.63	1958.23	3682.84	5407.44
Syn-	15029-1	H_2O	3	192	0.9857	0	0.0143	4.48	0.908	20.466	−1552.39	146.44	1845.28	3544.12	5242.95
Syn-	15029-14	H_2O	2	193	0.9870	0	0.0130	4.09	0.905	20.496	−1560.9	129.07	1819.05	3509.03	5199.01
Syn-	10029-14	H_2O	7	192	0.9878	0	0.0122	3.85	0.904	20.473	−1547.95	146.06	1840.07	3534.09	5228.10
Syn-	10029-1	H_2O	4	200	0.9901	0	0.0099	3.13	0.889	20.703	−1628.66	12.61	1653.88	3295.16	4936.43

Syn-: fluid inclusion that captured in quartz of syn-ore stage; n: the number of tested fluid inclusions; Th: finial homogenization temperature of fluid inclusion; H_2O: mole fraction of H_2O; XCO_2: mole fraction of CO_2; XNaCl: mole fraction of NaCl.

granite, and the quartz–pitchblende veins. However, the LREEs contents of the altered granites show richer than the unaltered granites.

The ΣREE contents of the quartz–pitchblende veins range from 19.2 to 681.75 ppb, the LREE/HREE ratios range from 0.57 to 5.17, the δEu values (calculated as $(Eu_{sample}/Eu_{C1Chondrite})/[(Sm_{sample}/Sm_{C1Chondrite} + Gd_{sample}/Gd_{C1Chondrite})/2]$) range from 0.21 to 0.48, and the δCe values (calculated as $(Ce_{sample}/Ce_{C1Chondrite})/[(La_{sample}/La_{C1Chondrite} + Pr_{sample}/Pr_{C1Chondrite})/2]$) range from 0.88 to 1.78. As shown in Fig. 15, ΣREE and δEu correlate positively with U content, while LREE/HREE and δCe correlate negatively with U content.

6.3. H–O isotopes

On the basis of fluid inclusion observations and quartz–water O-isotopic fractionation (e.g., Clayton et al., 1972), we were able to determine the $\delta^{18}O_W$‰ values of the ore-forming fluids. Our results are given in Table 3. The $\delta^{18}O_W$‰ values of the fluids involved in the uranium mineralization ranged from −1.8 to 5.4, with δD_W‰ values ranging from −104.4 to −57.2.

7. Discussion

7.1. P–T conditions of the uranium mineralization

Understanding the pressure and temperature conditions of the ore-forming fluids provides the foundation for studies of uranium transport and mineralization. Many researchers have studied the P–T conditions of uranium mineralization in the Changjiang uranium ore field through microthermometry (i.e., Chen and Liu, 1990; Zhang, 2008; Guo et al., 2010), but different conclusions have been reached. To produce a better analysis of the mineralization mechanisms, we made a series of micro-observations and conducted microthermometric analyses of the fluid inclusions.

Although the Laser Raman analysis suggested the occurrence of CH_4, H_2, and O_2, the microscopy observations and microthermometry work show that these volatiles are barely observed (i.e., the typical CH_4 clathrate). Therefore, the fluid inclusions were regarded as H_2O-type, CO_2-type and H_2O–CO_2-type generally.

The fluid inclusions of the syn-ore stage are characterized by the occurrence of CO_2, H_2O–CO_2, and H_2O inclusions in one cluster

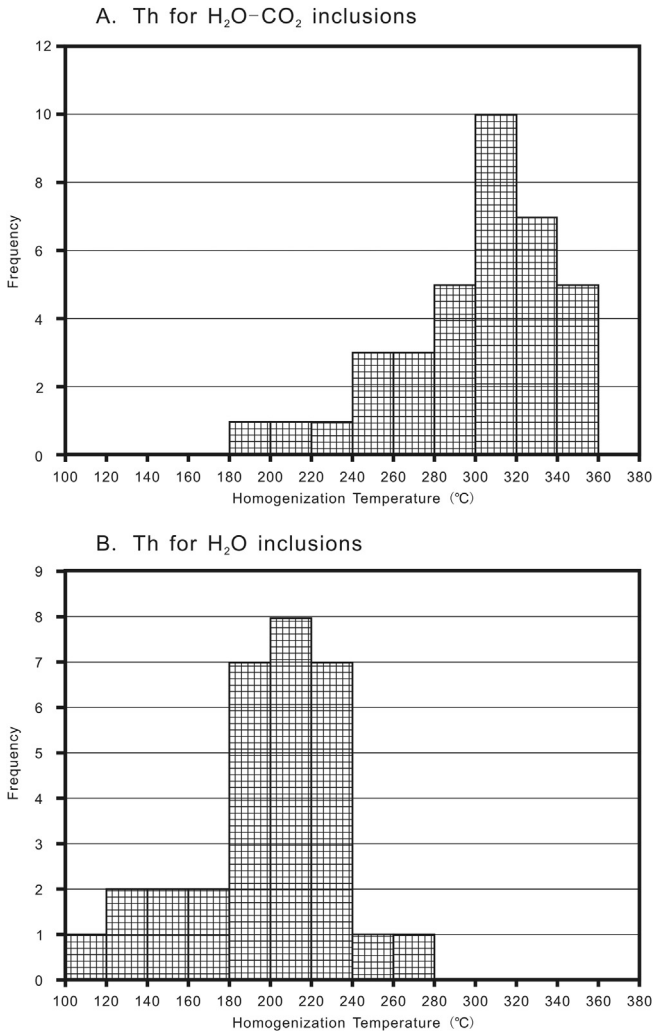

Fig. 10. Histograms of homogenization temperatures for H_2O-CO_2-type (A) and H_2O-type (B) fluid inclusions of syn-ore stage.

or trail, and this could be explained by three possible processes, as follows.

I Phase separation (or CO_2 effervescence) followed by heterogeneous entrapment of a CO_2-rich phase and a H_2O-rich phase as CO_2 inclusions of H_2O–CO_2 or H_2O inclusions, respectively, as has been suggested for gold deposits in Western Australia, Canada, and Egypt (e.g., Sherlock et al., 1993; Dugdale and Hagemann, 2001; Neumayr and Hagemann, 2002; Zoheir et al., 2008). Requirements of this process are that the CO_2, H_2O–CO_2, and H_2O inclusions occur in the same fluid inclusion assemblage, that they have widely varying degrees of fill and a small range of homogenization temperatures, and that pairs of liquid- and vapor-rich inclusions with opposite modes of homogenization (V → L and L → V) occur in the same assemblage of fluid inclusions (Ramboz et al., 1982; Lu et al., 2004).

II Mixing of fluids from two different sources, followed by entrapment of the mixtures as fluid inclusions (Xavier and Foster, 1999) and/or entrapment of different fluids at different times (Neumayr and Hagemann, 2002).

III Post-entrapment deformation that affects the fluid inclusions formed by the entrapment of a homogeneous (entirely miscible) phase at an earlier stage. In this process, deformation causes the inclusions to stretch, leak, or decrepitate, resulting in the preferential loss of H_2O and enrichment of the inclusions in CO_2 (e.g., Hall and Sterner, 1993; Bakker and Jansen, 1994; Johnson and Hollister, 1995; Kohtaro et al., 2008). The leaked H_2O-rich fluid is then trapped to form the H_2O inclusions.

The quartz grains in the veins of the Changjiang uranium ore field are characterized by a lack of post-mineralization deformation (e.g., undulatory extinction, banded extinction, and pressure solution seams), although some post-ore microfractures do occur. The fluid inclusion assemblage in the quartz veins is also characterized by a lack of post-entrapment deformation textures (e.g., necking down). These characteristics suggest that process III was not an option for the Changjiang uranium ore field.

If process II was active, the mixing of two separate fluids would have produced an array of fluid inclusions with widely variable $T_m(CO_2)$ and T_h values (reflecting variable compositions and temperatures of entrapment; e.g., Xavier and Foster, 1999). This is clearly not the case among the samples studied, which are characterized by uniform $T_m(CO_2)$ values and clustered T_h values.

We are led, therefore, to propose that process I was solely responsible for the formation of all types of fluid inclusions observed in the veins of the Changjiang uranium ore field. This is consistent with the common homogenization of inclusions through the disappearance of liquid or vapor phases, coupled with different degrees of fill for H_2O–CO_2 inclusions, as well as our observations that CO_2, H_2O–CO_2, and H_2O inclusions commonly coexist within one cluster or trail, suggesting they belong to the same fluid inclusion assemblage.

The H_2O inclusions are characterized by a nearly constant volume of the gas phase, approximately 10–15%, indicating the homogeneous entrapment of H_2O inclusions. Within a given sample, the difference in T_m(ice) of the H_2O inclusions is usually <2 °C (with one exception of 2.6 °C), corresponding to the salinity difference, which is typically less than 3 wt% NaCl equiv. In general, the salinities of the H_2O inclusions range from 2.39 to 5.55 wt% NaCl equiv., and the homogenization temperatures range from 106 to 254 °C, with peak values between 200 and 220 °C. These characteristics suggest that the H_2O inclusions were trapped within one phase field and that the pressures and temperatures of entrapment were not lower than the homogenization temperatures and pressures. The values of $T_m(CO_2)$ are generally between −57.4 and −58.0 °C, with differences less than 1 °C (although there is one exception at −61.0 °C); the CO_2 homogenization temperatures span from 17.8 to 22.1 °C. These features indicate another homogeneous trapped fluid inclusion, similar to the H_2O inclusions. The CO_2 and H_2O inclusions are end-members of a H_2O–CO_2 fluid, and during phase separation (or CO_2 effervescence), pairs of H_2O and CO_2 inclusions with different fill volumes of H_2O–CO_2 inclusions were trapped in a single fluid inclusion cluster or trail (Fig. 16).

The homogenization temperatures of H_2O inclusions range from 106 °C to 254 °C that are generally lower than the H_2O–CO_2, which range from 198 °C to 354 °C. These wide temperature ranges are probably due to the reequilibration after heterogeneous entrapment during CO_2 effervescence (Table 2), which also resulted in density variations between H_2O, CO_2 and H_2O–CO_2 inclusions. Isochores calculated from these microthermometric results for the H_2O and CO_2 inclusions have a consistent pressure when the temperature is between 200 and 300 °C. The average isochores of H_2O and CO_2 inclusions intersect at ~250 °C, with corresponding pressures of 1000–1100 bar (Fig. 17).

The $T_m(CO_2)$ of CO_2 and H_2O–CO_2 inclusions are lower than −56.6 °C, indicating that there is not only CO_2 in the gas but also O_2, CH_4, or H_2, consistent with the results of the laser Raman analysis. The clathrate melting temperatures range from 4.9 to 8.1 °C,

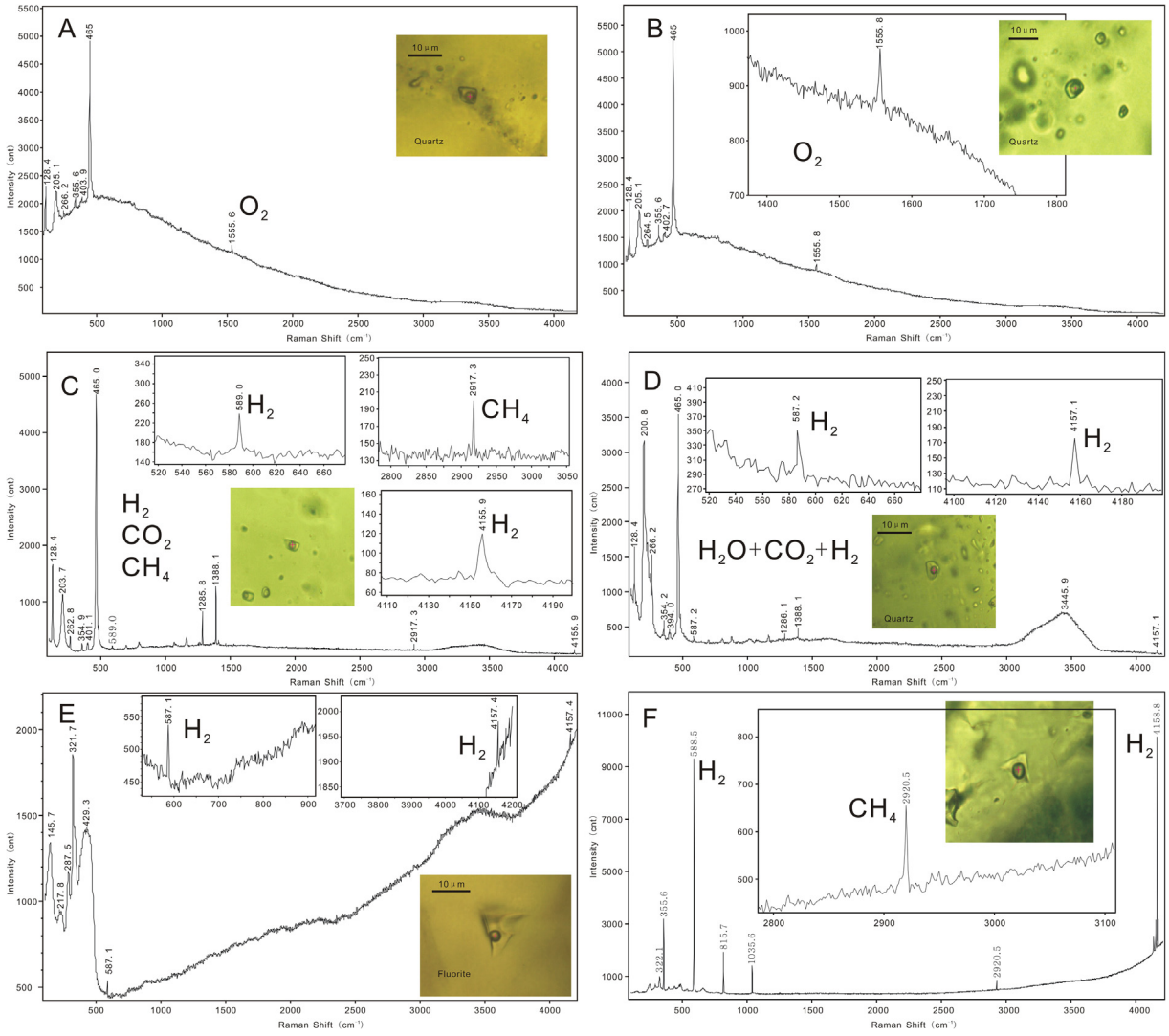

Fig. 11. Laser Raman analysis of fluid inclusions of the Changjiang uranium ore field. A. Laser Raman analysis of a H_2O-type fluid inclusion in a trail in altered granite, showing O_2 in the fluid inclusion (Sample 4–150-4, syn-ore stage). B. Laser Raman analysis of a H_2O-CO_2-type fluid inclusion located in a cluster in a quartz-pitchblende vein, showing that O_2 occurs in the fluid inclusion (Sample ZN10, syn-ore stage). C. Laser Raman analysis of a H_2O-CO_2-type fluid inclusion located in a cluster in a quartz-pitchblende vein, showing the presence of CO_2, H_2 and CH_4 in the fluid inclusion (Sample 15029–1, syn-ore stage). D. Laser Raman analysis of a H_2O-CO_2-type fluid inclusion located in a cluster in a quartz-pitchblende vein, showing the presence of H_2 in the fluid inclusion (Sample 15029–14, syn-ore stage). E. Laser Raman analysis of a H_2O-CO_2-type fluid inclusion located in fluorite vein, showing that H_2occurs in the fluid inclusion (Sample 4–150-9, CJ-QY-17, post-ore stage).F. Laser Raman analysis of a H_2O-CO_2-type fluid inclusion located in a fluorite-quartz vein, showing the presence of H_2 and CH_4 in the fluid inclusion (Sample 4–150-9, CJ-QY-17, post-ore stage).

corresponding to salinities between 3.76 and 9.24 wt% NaCl equiv., which are slightly higher than those for the H_2O inclusions. The CO_2 homogenization temperatures range from 24.5 to 30 °C, and the total homogenization temperatures span from 198 to 354 °C, with peak values between 300 and 320 °C. The H_2O–CO_2 inclusions were trapped in a two-phase field, meaning that the entrapment temperatures and pressures were lower than the homogenization temperatures and pressures, which indicates that an entrapment temperature of ~250 °C and a pressure of ~1100 bar are reliable figures. Based on these observations, we assumed that the mineralization temperature was 250 °C, and this value is used in the following H–O isotope study.

There are three possible explanations for the observed phase separation (or CO_2 effervescence): 1) a decompression effect in which the pressure dropped below the boiling pressure with constant temperature, 2) the injection of a low-temperature fluid, or 3) a combination of these two. The Changjiang uranium ores occur mainly along ~N–S striking faults that are characterized by extension, and the phase separation or CO_2 effervescence probably have resulted from the decompression effect of that extension (Sibson, 2004; Faleiros et al., 2007). The decompression would have resulted in a drop in confining pressure of the ore-forming fluid, and this would have been reflected in a decrease in the homogenization temperature. The different amounts of CO_2 fill in CO_2-bearing inclusions whereas constant H_2O fill in H_2O inclusions suggest that the confining pressure after decompression could probably be lower than the pressure point of CO_2 effervescence, but higher than H_2O boiling (Sibson, 2001). In general, such a decompressional event would have led to a large variation in the range of homogenization temperatures for fluid inclusions in the Changjiang uranium ore field.

7.2. Geochemical properties of ore-forming fluids

In addition to the P–T conditions, the geochemical properties of the ore-forming fluids are also important in controlling uranium

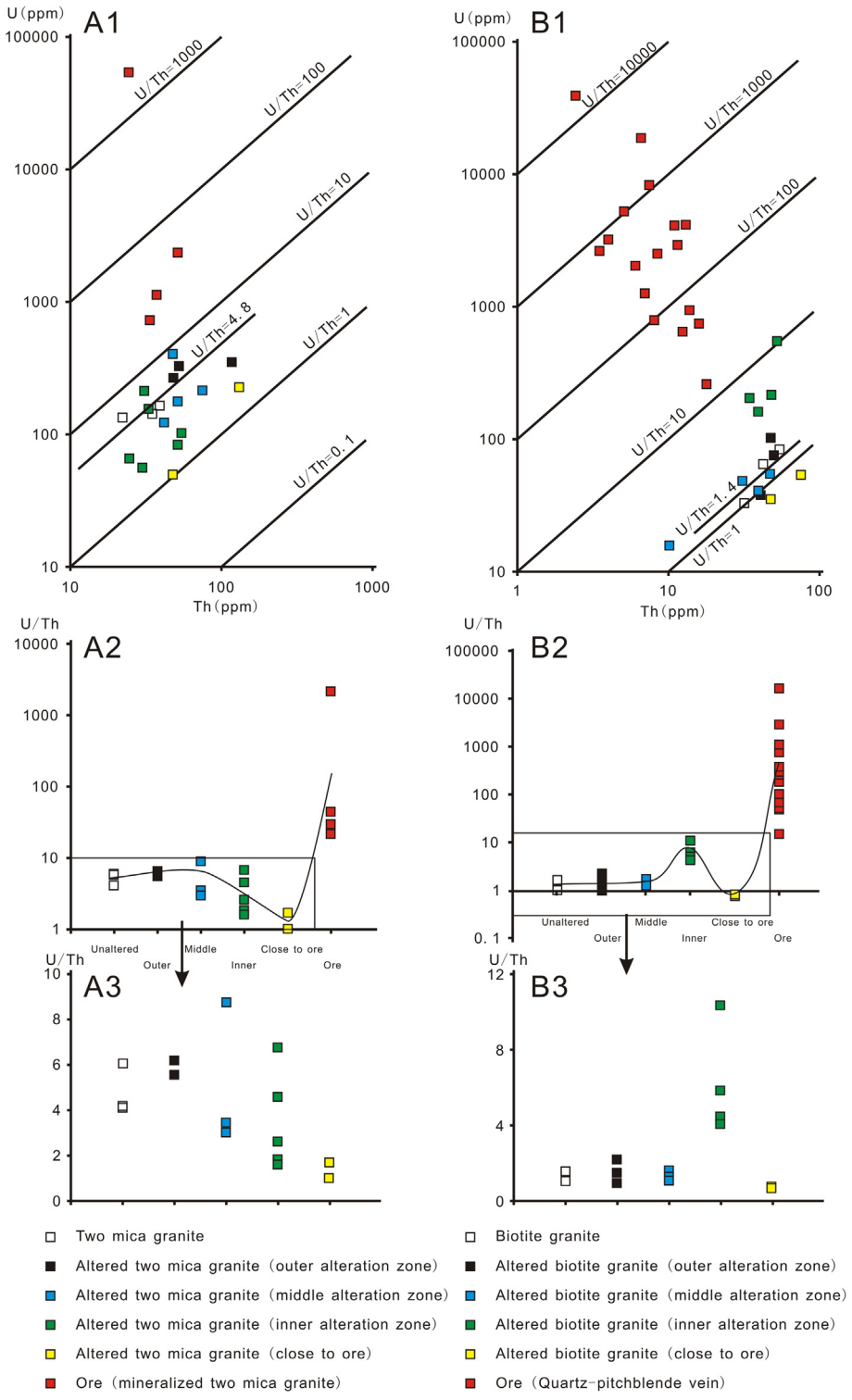

Fig. 12. U and Th contents, and U/Th values of unaltered and altered granite and ore. A1. U and Th contents of mineralized, altered, and unaltered two-mica granite. A2. U/Th value diagrams of mineralized, altered, and unaltered two-mica granite. A3. Detailed view of the area marked by a rectangle in A2. B1. U and Th contents of altered and unaltered biotite granite and quartz-pitchblende vein. B2. U/Th value plots of altered and unaltered biotite granite and quartz-pitchblende vein. B3. Detailed view of the area marked by a rectangle in B2.

transportation, hydrothermal alteration, and mineralization mechanisms. Jin and Hu (1987) proposed that the Changjiang ore-forming fluids were characteristically oxidizing and acidic, but this statement was questioned by Ni et al. (1994), who suggested the fluids were reducing, as indicated by CH_4-containing fluid inclusions. These opposing views motivated us to focus on the geochemical characteristics of the fluid inclusions. Bearing in mind the mineral paragenesis outlined above, we attempted to determine the geochemical properties of the ore-forming fluids and the post-ore hydrothermal fluids by conducting laser Raman and

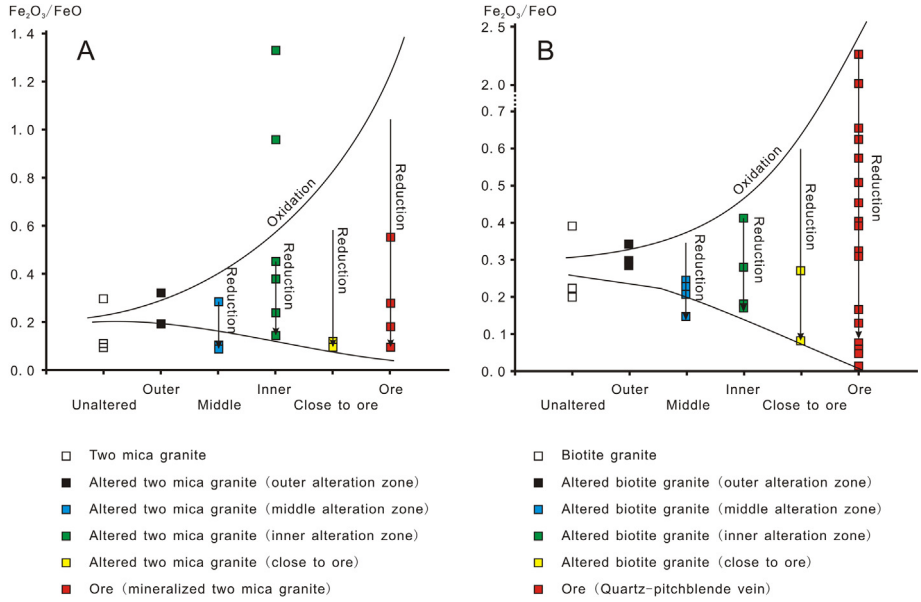

Fig. 13. A. Fe_2O_3/FeO value plots of mineralized, altered, and unaltered two-mica granite. B. Fe_2O_3/FeO value plots of altered and unaltered biotite granite and quartz-pitchblende vein.

microthermometry analyses of fluid inclusions from quartz–pitchblende veins, fluorite–quartz veins, and altered granites adjacent to the ore-bearing faults.

The Laser Raman analysis of fluid inclusions in syn-ore stage minerals indicates the presence of two types of fluid inclusion. In the first type, the fluid inclusions contain O_2, indicating the entrapment of oxidizing fluids in the inclusions, whereas the second type contains CH_4 and H_2, which indicate the presence of reducing fluids. It seems at first to be a contradiction that these two types of fluid inclusion could occur in the same mineral unless they were entrapped at different times. There are, however, four possible explanations for this phenomenon, as follows.

I Both types of fluid inclusions were entrapped simultaneously, and were the mixing result of two types of fluid (one containing O_2 whereas the other CH_4 and H_2) during the mineralization event. In this mixture, there is at least one type of inclusion that contains CO_2. This mixture could explain the occurrence of CO_2, H_2O–CO_2, and H_2O fluid inclusions in one cluster or trail, with the CO_2 contents ranging from 20 to 80 vol% in the H_2O–CO_2 inclusions. In such a mixture, one phenomenon should be observed: in any one cluster or trail, there should be two types of inclusions, one containing O_2, the other H_2–CH_4, but this was not observed. The homogenization temperatures should vary widely, with different salinities and pressures, but the microthermometry results do not indicate such variations. Thus, this explanation can be rejected with respect to the Changjiang uranium ore field.

II The two types of fluid inclusion were entrapped at different substages, but all within the syn-ore stage. The inclusions that contained O_2 would have formed earlier than those containing CH_4 and H_2, and both fluids would have been characterized by high CO_2 contents. There are many possible reasons for a change from an oxidizing to a reducing fluid, such as water (oxidizing)–rock (reducing) interactions or the injection of a reducing fluid.

III The inclusions that contained H_2 and CH_4 formed earlier than those containing O_2, and both fluids were characterized by high CO_2 contents. Because of the reducing property of the wall rock, it is difficult for a reducing fluid to become oxidizing through water–rock interactions, but the injection of an oxidizing fluid could be a possible explanation for such a change.

IV The syn-ore stage inclusions that contain H_2 and CH_4 could possibly be derived from post-ore stage fluids that were overprinted on syn-ore minerals, or through the H_2 and CH_4 diffusion under a chemical gradient between trapped fluid (syn-ore stage) and an external circulating fluid (post-ore stage, re-equilibration of fluid inclusions) (Dubessy et al., 1988), and evidence of this might be provided by the inclusions (second type) that occur in the post-ore stage. Because of the similar CO_2 contents and fluid inclusion assemblages in the syn-ore and post-ore stages, and the fact that some of the assemblages occur in microfractures in the altered granites and veins, we consider it is possible that some fluid inclusions of the second type were entrapped during the post-ore stage.

To further explore explanations II, III, and IV, we collected samples with and without post-ore veins (fluorite veins, calcite–quartz veins), and subjected them to laser Raman analysis. The results show that the samples with post-ore veins contain more second type inclusions than those without post-ore veins, which suggest that most of the CH_4- and H_2-containing inclusions formed in post-ore stage with a few others probably forming in syn-ore stage or through H_2 and CH_4 diffusion of post-ore fluid into syn-ore inclusions (Dubessy et al., 1988).

The fluid inclusions of the second type from the syn-ore stage were probably entrapped later than the first type, and at a time that can be considered to be the post-ore stage. The foregoing results indicate that the ore-forming fluids were oxidizing in the early syn-ore stage but changed to reducing during the late syn-ore and post-ore stages. This would have resulted in a decrease in uranium solubility in the ore-forming fluids, thus implying an end to the uranium mineralization. This deduction is supported by a geochemical analysis of the hydrothermal alteration, as detailed in the following section.

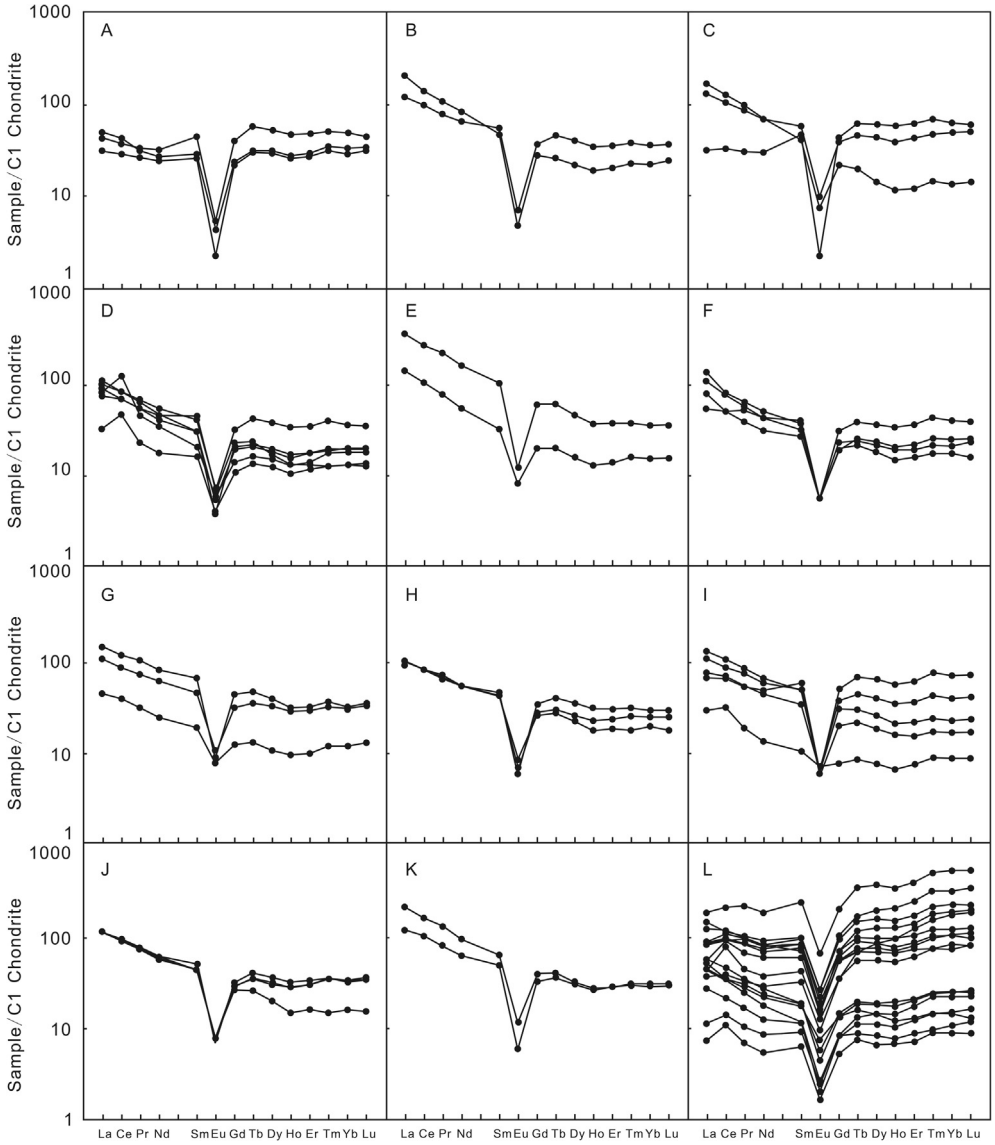

Fig. 14. REE patterns of different samples normalized to chondrites. A. Unaltered two-mica granite. B. Altered two-mica granite from outer alteration zone. C. Altered two-mica granite from middle alteration zone. D. Altered two-mica granite from inner alteration zone. E. Altered two-mica granite close to ore. F. Mineralized two-mica granite. G. Unaltered biotite granite. H. Altered biotite granite from outer alteration zone. I. Altered biotite granite from middle alteration zone. J. Altered biotite granite from inner alteration zone. K. Altered biotite granite close to ore. L. Quartz-pitchblende vein.

7.3. Hydrothermal alteration

Following on from our determination of the physical and geochemical characteristics of the ore-forming fluids, a study of the hydrothermal alteration would be possible after determining the chemical constituents of the unaltered and altered wall rocks. Hydrothermal alteration is the result of interactions between the rocks and hydrothermal fluids (ore-forming fluids), and understanding the nature of this alteration is essential for studies of mineralization mechanisms, because the reactions during alteration cause variations in the chemical properties of the hydrothermal fluid, which might lead to ore deposition (Robb, 2005). Previous studies examined the process of hydrothermal alteration in the Changjiang ore field (Gao et al., 2011a, b; Wang and Ding, 2007), but failed to consider the properties of the ore-forming fluids and lack a thorough analysis. Moreover, their conclusions are contradictory.

The fluid inclusion studies outlined above have provided clues to the process of hydrothermal alteration in the Changjiang uranium ore field. The wall rocks near ore-bearing faults have undergone two stages of alteration: syn-ore and post-ore. The early syn-ore alteration was characterized by interactions between oxidizing ore-forming fluids and the granite, and the late syn-ore and post-ore alterations were characterized by interactions between reducing fluids and altered granite. To understand the alteration processes and the mineralization mechanisms more clearly, we have analyzed the geochemical data (presented in Appendix C) pertaining to the wall rocks in the Changjiang uranium ore field.

7.3.1. Uranium migration

In the Changjiang ore field, uranium is the most important ore element, therefore, we have subjected it to analysis first. The aqueous geochemistry of U is unusual in that U is generally more soluble in oxidizing and carbonate-rich water than in reducing

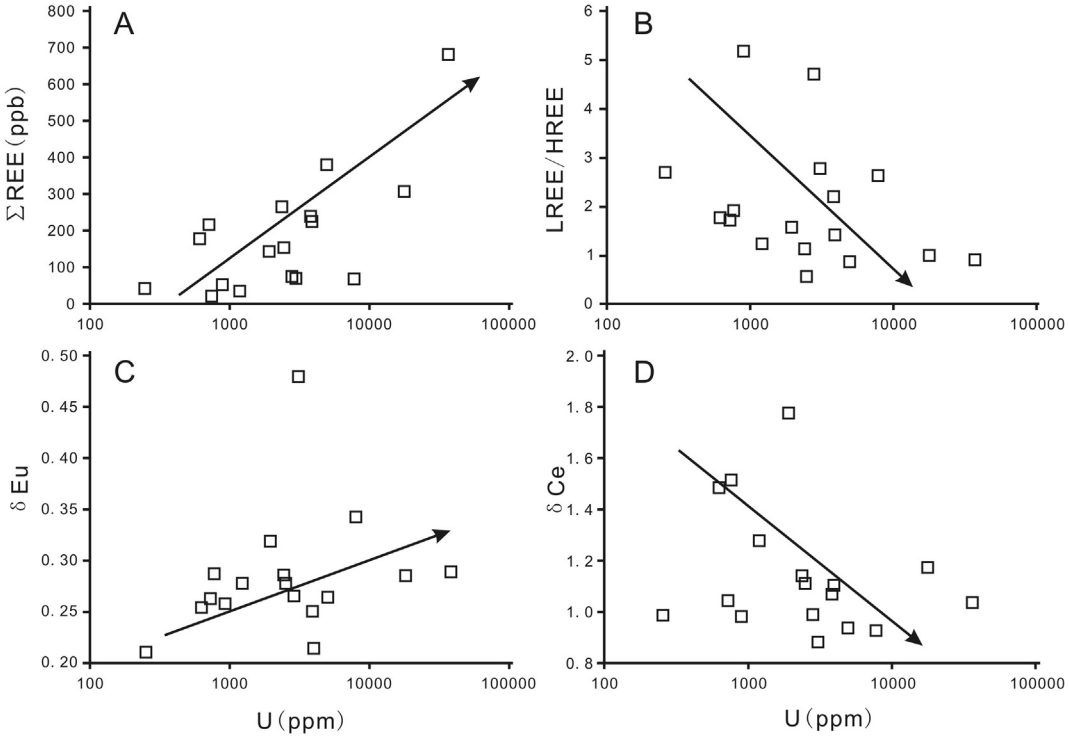

Fig. 15. ΣREE (A), LREE/HREE (B), δEu (C), and δCe (D) values vs. U content for quartz-pitchblende veins in the Changjiang uranium ore field.

Table 3
Oxygen and Hydrogen isotopic compositions of quartz-pitchblende veins from the Changjiang uranium ore field.

Sample No.	Petrology	Mineral	$\delta D_{V\text{-}SMOW}$	$\delta^{18}O_{V\text{-}PDB}$	$\delta^{18}O_{V\text{-}SMOW}$	$\delta D_{W\text{-}SMOW}$	$\delta^{18}O_{W\text{-}SMOW}$	Resources
ZN3	Quartz-pitchblende vein	Quartz	−84.2	−22.2	8	−84.2	−0.9	This study
ZN3-1	Quartz-pitchblende vein	Quartz	−73.9	−19.8	10.5	−73.9	1.6	
ZN10	Quartz-pitchblende vein	Quartz	−73.4	−23.1	7.1	−73.4	−1.8	
ZN14	Quartz-pitchblende vein	Quartz	−57.2	−19	11.3	−57.2	2.4	
ZN33-1	Quartz-pitchblende vein	Quartz	−104.4	−16.1	14.3	−104.4	5.4	
ZN42-6	Quartz-pitchblende vein	Quartz	−85.2	−18.8	11.5	−85.2	2.6	
ZN45-1	Quartz-pitchblende vein	Quartz	−58.5	−23.1	7.1	−58.5	−1.8	
15029-1	Quartz-pitchblende vein	Quartz	−77.9	−21.5	8.7	−77.9	−0.2	
5008-3	Quartz-pitchblende vein	Quartz	−71.6	−20.1	10.2	−71.6	1.3	
10041-1	Quartz-pitchblende vein	Quartz	−92.2	−20.4	9.9	−92.2	1.0	
10029-1	Quartz-pitchblende vein	Quartz	−51.6	−20.6	9.7	−51.6	0.8	
04C-2	Quartz-pitchblende vein	Quartz	−71.5	−19.5	10.8	−71.5	1.9	
3-62	Quartz vein	Quartz	−74		11.2	−74	2.3	Zhang (2008)
2-04	Quartz vein	Quartz	−76		9.9	−76	1.0	
2-71	Quartz vein	Quartz	−85		10.1	−85	1.2	
2-75	Quartz vein	Quartz	−83		9.8	−83	0.9	
2-78	Quartz vein	Quartz	−88		10.6	−88	1.7	

Note: $1000 \ln \alpha_{V\text{-}W} = 3.38 \times 10^6 T^{-2} - 3.40$ (200–500 °C; T = 250 °C) (Clayton et al., 1972).

water. This peculiarity is due primarily to the tendency of U^{6+} to form strong complexes in oxidizing fluids, regardless of temperature (Cuney and Kyser, 2008). Thorium, which has the same ionic radius as uranium and exists only in a tetravalent state in natural systems, behaves in a similar way to uranium in all magmatic fractionation processes. Uranium is characterized by a high solubility in fluids with high oxygen fugacities, but a low solubility in fluids with low oxygen fugacities. In contrast to uranium, the solubility of thorium is low in both oxidizing and reducing hydrothermal fluids. These observations suggest that we should use U/Th ratios to evaluate the variations in uranium when granites are affected by hydrothermal alteration.

One significant characteristic of the ore-forming fluids in the Changjiang uranium ore field that differentiates them from most other modern systems, but is shared with unconformity-type uranium deposits, is their high oxidation state, as indicated by the O_2 contents in fluid inclusions of the early syn-ore stage. In contrast to the ore-forming fluids of the early syn-ore stage, the late syn-ore and post-ore fluids were reducing, as indicated by the H_2 and CH_4 contents of the fluid inclusions. These characteristics suggest that the U contents of the Changjiang ores were affected mainly by oxidizing fluids of the early syn-ore stage, and only slightly by later reducing fluids, and that the Th contents of the altered granites were controlled mainly by the formation of the granites, with little effect from the later oxidizing and reducing hydrothermal fluids. Regarding the U contents of the altered granites, there are two factors that should be considered: the formation of the granites, and the alteration due to oxidizing fluids.

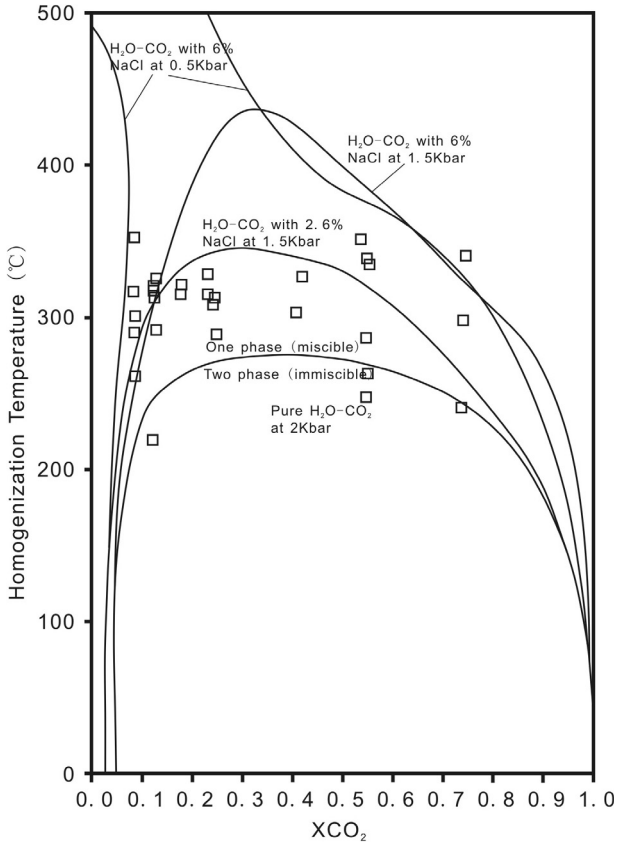

Fig. 16. Homogenization temperature vs. XCO_2 plots for H_2O-CO_2-type fluid inclusion, showing that phase separation or CO_2 effervescence of ore-forming fluid is possible.

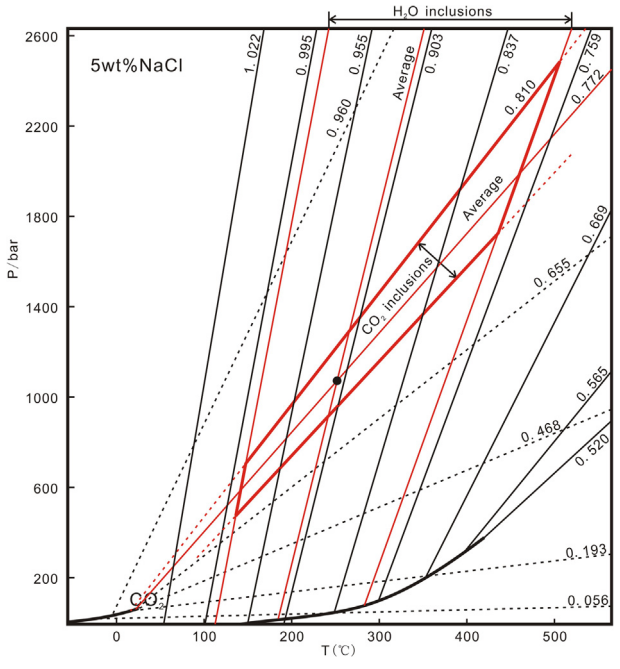

Fig. 17. Pressure–temperature plots for CO_2- and H_2O-type inclusions, showing that the mineralization temperatures are approximately 250 °C, with corresponding pressures of 1000–1100 bar (Bodnar and Vityk, 1994; Angus et al., 1979).

In the alteration profile of the two-mica granite, changes in U/Th values occur regularly from the unaltered to the mineralized granite zone (Fig. 12). The U/Th values of the outer alteration are slightly higher than those of the unaltered two-mica granite, but through the middle and inner alteration zones, and closer to the ore, they become increasingly lower. The U/Th values in the unaltered two-mica granite are ~4.8 on average, and this represents the U/Th value without any later hydrothermal alteration. The U/Th values in the altered granites that lie close to the ore are much lower than 4.8, indicating loss of uranium during hydrothermal alteration. With respect to the middle and outer alteration zones, the U/Th values are slightly higher than 4.8, meaning uranium was added during the hydrothermal alteration. These observations suggest that the ore-forming fluids of the early syn-ore stage transported uranium from the two-mica granite close to the faults and deposited it in the middle and outer alteration zones during the process of alteration.

In contrast to the U/Th values in the two-mica granite, the values in the outer and middle alteration zones of the biotite granite are nearly the same as those measured in the unaltered granite, which is ~1.4 on average, and the U/Th values in the inner alteration zone are much higher than those in the outer and middle alteration zones, indicating the addition of uranium during hydrothermal alteration. When close to the quartz–pitchblende veins, the U/Th values become much lower than those observed in the inner alteration zone, which are slightly lower than 1.4, suggesting the loss of uranium. These observations suggest that the ore-forming fluids of the early syn-ore stage transported uranium from the biotite granite close to the faults, and deposited it in the inner alteration zones.

Comparisons between the altered two-mica granite and altered biotite granite show that both types of granite share some similarities, such as the loss of uranium in the altered granites close to the faults, and deposition of uranium in the alteration zones located close to the zone of uranium loss. Comparisons of the U and Th content, and U/Th values of the unaltered and altered granites indicate that some uranium was derived from the altered granites close to the faults, but that more uranium resources were added to the altered granites during alteration, which implies that the oxidizing ore-forming fluids carried uranium from other areas.

7.3.2. Temporal variations in oxidation state

The ore-forming fluids of the early syn-ore stage were characterized by high oxidation states, and the fluids of the late syn-ore and post-ore stages were characterized by being reducing. This switch suggests that the variations in oxidation of the altered granites when they underwent hydrothermal alteration could be represented by variations in Fe^{3+}/Fe^{2+}.

In the Changjiang ore field, there are four main types of minerals containing Fe: biotite, chlorite, pyrite, and hematite. These minerals have two different valency states: Fe^{3+} and Fe^{2+}. Biotite is a magmatic mineral, while the others are the products of alteration. When the granites underwent oxidizing (early syn-ore) alteration, the biotites were at least partially altered to chlorite, and this alteration was accompanied by the development of hematite and the conversion of some Fe^{2+} to Fe^{3+}. After this oxidizing alteration, the wall rocks underwent a reducing alteration, and pyrite was developed in the ores and altered granites. During the alteration, some of the hematite was transformed to pyrite, which means that some Fe^{3+} was converted to Fe^{2+}, according to the reaction shown below.

$$Fe_2O_3 + H_2 + CH_4 + S^{2-} \rightarrow FeS_2 + H_2O + CO_2$$

As shown in Fig. 13, the minimum values of Fe_2O_3/FeO decrease as the maximum values increase from the unaltered granites to the ores, suggesting that granites near the faults underwent oxidation first and reduction second, in agreement with our studies of the

fluid inclusions. During the alteration that occurred at the early syn-ore stage, the biotites in the granites were altered to chlorite and hematite (the latter forming layers along the foliations of the chlorite), indicating that most Fe^{2+} in the biotite was converted to Fe^{3+} so that the values of Fe_2O_3/FeO increased with the degree of alteration. During the late syn-ore and post-ore alterations, the granites near the faults underwent a reducing alteration, characterized by the development of pyrite in the altered rocks. This implies that either some Fe^{3+} was converted to Fe^{2+} and/or that new Fe^{2+} was introduced into the system, and the values of Fe_2O_3/FeO consequently decrease with the increasing degree of alteration. The Fe_2O_3/FeO values vary significantly among samples, even within a single alteration zone, and this probably indicates that even in a single alteration zone the rocks underwent varying degrees of alteration.

7.3.3. Variations in REE contents

In addition to U, Th, and Fe, the REE variations during uranium mineralization and alteration should also be analyzed. The REE contents of the two-mica granites and biotite granites show some differences. With regard to the two-mica granites, the altered samples are richer in LREEs than are the unaltered samples, but for the biotite granites the REE diagrams are similar for both unaltered and altered types. Variations in the REE contents of the altered granites were generated as a result of syn-ore and post-ore alteration, and by way of contrast, the REE contents of the quartz–pitchblende veins (formed during the syn-ore stage) only experienced the effects of post-ore alteration. The post-ore fluids were reducing and are likely to have had only a minimal effect on the quartz–pitchblende veins, leaving their REE contents fairly constant during later periods of alteration.

The early syn-ore oxidizing fluids played an essential role in establishing the REE patterns for the pitchblende veins, which are made up mainly of REE-hosting minerals that were only slightly affected by the later reducing fluids. The REE patterns for the quartz–pitchblende veins can be divided into two groups: patterns of the first group are similar to those of altered granites, and can be characterized as LREE-rich, whereas the second group can be characterized as HREE-rich (Fig. 14).

As shown in Fig. 15, ΣREE increases but LREE/HREE ratios decrease with increasing U content. The positive correlation between U contents and ΣREE suggests that the REEs are concentrated mainly in the pitchblende. The negative correlation between U contents and LREE/HREE ratios indicates that the pitchblende is relatively rich in HREEs. Compared with pitchblende from elsewhere with higher REE abundances ($\times 10^4$ chondritic abundance for most of the REEs, due to the increased substitution of REEs into the uranium oxide crystals at high temperatures), the pitchblende veins at Changjiang are characterized by relatively low total REE abundances (<1000 chondritic abundance for most of the REEs), implying that the Changjiang veins crystallized at relatively low temperatures (Bonhoure, 2007; Cuney, 2010), which is consistent with our analyses of fluid inclusions.

The REE patterns of the quartz–pitchblende veins with low ΣREE show a typical magmatic signature, while the high ΣREE ones show a pattern similar to average seawater and river water (Elderfield and Greaves, 1982), which suggest that the ore-forming fluid should be genetically related to ground water, in accordance with H–O isotopes (see details in 7.4). Compared with the pitchblende in unconformity-related deposits that crystallized at lower temperatures, the one in Changjiang should have been deposited at low-moderate temperatures, as shown by fluid inclusion research (Bonhoure, 2007; Cuney, 2010).

The altered granites, especially those close to the faults, underwent two stages of alteration: an early syn-ore oxidizing stage and a late syn-ore and post-ore reducing stage. The REE diagrams of the altered granites are the result of a combination of magmatism and syn-ore and post-ore alteration, but it is difficult to identify the roles of each geological event.

Eu is an element with variable valency, although usually trivalent along with other REEs, and this allows it to migrate with the other REEs; however, in a reducing environment, some Eu^{3+} is converted to Eu^{2+} and separated from the other REEs, which would produce an Eu anomaly. In contrast to Eu, Ce^{3+} would be converted to Ce^{4+}, which would form CeO_2 in an oxidizing environment and result in its separation from the other REEs (Han et al., 2003). As shown in Fig. 14, in pitchblende–quartz veins, δEu has a positive correlation with U whereas δCe has a negative correlation, implying the mineralization environment changed from oxidizing to reducing (Han et al., 2003), in agreement with our fluid inclusion research. However, the positive δCe anomalies of some altered granites probably resulted from late syn-ore and post-ore alteration, or an anomalous La enrichment (Planavsky et al., 2010).

7.4. Origin of the ore-forming fluids

With regard to the origin of the ore-forming fluids in the Changjiang ore field, previous researchers have suggested they were a mix of magmatic and meteoric waters (Du and Wang, 1984; Hu et al., 1993; Min et al., 1999, 2005), or sourced from the mantle (Deng et al., 2003; Jiang et al., 2004; Zhu et al., 2006; Wang and Li, 2007), based on H–O isotopic studies. Furthermore, previous researchers identified four ages (U–Pb dating of pitchblende) for the uranium mineralization in the Changjiang ore field: 127 Ma (Zhang, 2008), 82–87 Ma (Zhang, 2002), 73–75 Ma (Zhang, 2002), and 54 Ma (Zhang, 2008), all of which suggest that the uranium mineralization occurred mainly during the Cretaceous–Paleogene, and may have extended over tens of millions of years. During the Cretaceous–Paleogene, intermontane sedimentary basins were formed in the region, but there was practically no magmatism or metamorphism, which means it is difficult to infer whether the ore-forming fluids were a mixture of magmatic and meteoric fluids. The δD‰ values of meteoric water in the study area during the Cretaceous–Paleogene range from −30 to −70, and the $\delta^{18}O$‰ values range from −5 to −10. The $\delta^{18}O_W$‰ values for the ore-forming fluids range from −1.8 to 5.4, and the δD_W‰ values range from −104.4 to −57.2, and these values are vastly different from those measured for meteoric water, but similar to those measured for basinal fluids (Fig. 18). The $\delta^{18}O$ values of the ore-forming fluids were too low for them to have been sourced from metamorphic fluids, and normal magmatic sources are ruled out by the δD values (Taylor, 1987), thus ruling out a basement-derived ore-forming fluid. Fluid inclusions of the syn-ore stage always contain certain amounts of O_2, which suggests that the ore-forming fluids were exposed to the atmosphere (as would have been the case with meteoric water or basinal fluids). However, the H_2 that in syn-ore stage inclusions could not be explained by the exposure to the atmosphere. According to Dubessy et al. (1988), the H_2 could be produced in the presence of water and/or organic matter when chain fission reactions occur, or generated by redox processes during interactions between ground water and strong reducing matter (i.e., H_2 is commonly found in oil fields, Zinger, 1962; Nechayeva, 1968; Neal and Stranger, 1983). Considering the nonexistence of chain fission reactions and the presence of CH_4-containing inclusions in Changjiang, the redox processes are preferred to be the best explanation for the H_2 occurrence, the reducing matter is probably the black shale which is present intercalated with red beds in basins and ore-hosting granites, in both of which have the regional faults acted as channel ways for fluids.

During discussing the origin of the ore-forming fluids, the interactions between those fluids and the ore-hosting rocks should also be considered. The geochemical data related to the ores and altered

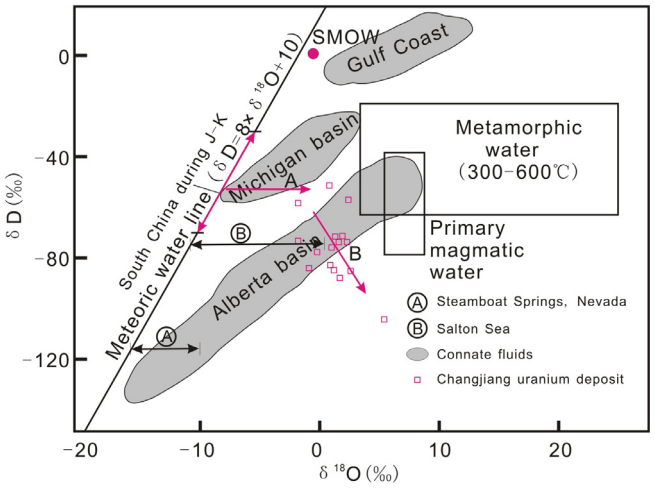

Fig. 18. Oxygen and hydrogen isotopic plots of the Changjiang uranium ore field (Zhang et al., 1995).

granites indicate that only granites close to the ores underwent loss of uranium, and altered granites that are close to uranium-loss zones are richer in uranium after alteration. Clearly, the loss of uranium from the altered granites cannot match the known reserves of uranium in the Changjiang ore field. All these observations indicate that the syn-ore alteration involved the addition of uranium, and that the altered granites were responsible for only a small proportion of the uranium present in the ore field. Moreover, the fluids contained uranium, as indicated by the O_2 contents of fluid inclusions, indicating that the fluids had a high uranium solubility.

The water–rock interactions during the syn-ore stage occurred mainly along ~N–S striking faults, indicating that this system was probably an open, naturally buffered system. We suggest that the mineralization required a lasting input of uranium-bearing fluids, even though the solubility of uranium in the oxidized ore-forming fluids was high at this stage. A naturally buffered system is indicated by the H–O isotopes, shown as trend B on Fig. 18. In such a system, when the oxidized uranium-bearing fluids were transported into the ~N–S trending faults, they would have reacted with the granites, resulting in the transformation of biotite to chlorite together with hematite. This reaction was characterized by the conversion of Fe^{2+} to Fe^{3+} and the consumption of O_2 in the ore-forming fluids, thus leading to a decrease in oxygen fugacities, and this would have decreased the solubility of uranium in the fluids, allowing for the precipitation of uranium.

If the ore-forming fluids were initially meteoric water, this water must have experienced at least one stage of water–rock interaction to obtain the uranium dissolved in the fluid before the syn-ore alteration, for there would have been no uranium in the original meteoric water. As a result of the low H contents but high O contents of the rock, as indicated by trend A in Fig. 18, this pre-ore stage water–rock interaction would have produced a positive change in $\delta^{18}O‰$ with a small change in the δD‰ value of the ore-forming fluids. In the pre-ore stage of water–rock interaction, the meteoric water would also have obtained substantial amounts of dissolved CO_2, which would have made it different from the original meteoric water.

The ore-forming fluids could also have been basinal fluids, as supported by the fact that the H–O isotopes plot in the basinal fluid field in Fig. 18. The formation of an inter-continental sedimentary basin during the Cretaceous–Paleogene indicates that this inference is reasonable. Initially, the basinal fluids would have been mainly meteoric water, characterized by high oxygen fugacities that would have enabled the fluids to easily extract uranium from terrigenous clasts through water–rock interactions (Kyser et al., 2000), because the clasts would have been characterized by high surface areas of 5–7 orders of magnitude higher than that of the granite body. From the sedimentary basin to the location of mineralization, the ore-forming fluids may have traveled through metamorphic basement rocks (Fig. 2), where they could have obtained uranium and CO_2 through water–rock interactions (Cuney et al., 2003).

7.5. Mineralization mechanism

Here we provide a discussion of the mineralization mechanism, based on our determination of the P–T conditions, the geochemical properties and origins of the ore-forming fluids, and our understanding of the interactions between the ore-forming fluids and the ore-hosting rocks.

It is unlikely that the granite was the source of the uranium. Previous studies have indicated that low-to medium-K calc-alkaline granites are never associated with U mineralization (Cuney and Kyser, 2008), because most of the U is hosted by refractory accessory minerals. Similarly, high-K calc-alkaline granites, which have high U (12–20 ppm) and Th (30–60 ppm) contents, are not directly associated with U deposits (Pagel, 1982), because the U is mainly hosted in uranothorite (U, Th)SiO_4 that is highly resistant to leaching when hydrothermal circulation takes place some tens of millions years after granite emplacement (Pagel, 1982; Cuney and Friedrich, 1987).

Uranium is immobile in reducing groundwater with pH levels between 4 and 8, and low Eh values, and it has a minimal temperature dependence from 100 to 300 °C (Parks and Pohl, 1988; Shock et al., 1997). However, in environments with higher Eh values, oxidation of uraninite and coffinite can increase solubility by several orders of magnitude, particularly when phosphate and carbonate are present (Cuney and Kyser, 2008). In basinal brines, uranyl carbonate complexes ($UO_2(CO_3)^{2-}$) are dominant under relatively oxidizing and near-neutral pH conditions, and UO_2Cl- is dominant in fluids under acidic conditions at temperatures up to 200 °C (Romberger, 1984; Kojima et al., 1994). As temperatures increase, carbonate complexes become less important, while hydroxide complexes become dominant (Romberger, 1984). In the Changjiang uranium ore field, uranyl carbonate complexes $UO_2(CO_3)^{2-}$ probably dominated under a relatively oxidizing environment with near-neutral pH conditions, which is indicated by the high O_2 and CO_2 contents of the fluid inclusions. There are two mechanisms that can lead to uraninite precipitation: the release of CO_2 and the reduction of U^{6+}. Based on the analysis given above, we know that CO_2 effervescence occurred during the uranium mineralization, which would have resulted in a marked fall in the CO_2 content of ore-forming fluids and a decrease in the solubility of U^{6+}. In addition, the reduction of U^{6+} through reaction with Fe^{2+} (biotite in granite) could also be the mechanism of uraninite precipitation, according to the following reactions.

$$\text{Biotite} + O_2 + U^{6+} \rightarrow \text{Chlorite} + UO_2(\downarrow) + Fe_2O_3(\downarrow)$$

$$K\{(Mg_{<0.67}, Fe_{>0.37})_3[AlSi_3O_{10}](OH)_2\} + O^2 + U^{6+} \rightarrow (R^2+, R^{3+})_{5\sim6}[(Si, Al)_4O_{10}](OH)_8 + UO_2(\downarrow) + Fe_2O_3(\downarrow)$$

$$(R^{2+} = Mg^{2+}, Fe^{2+}, Mn^{2+}, Ni^{2+}; R^{3+} = Al^{3+}, Fe^{3+}, Cr^3+, Mn^{3+})$$

If the pH were low, UO_2Cl^- would have been dominant in the fluids, and therefore U^{6+} reduction by reaction with Fe^{2+} would be the most likely mechanism that led to the precipitation of uraninite. In summary, the mechanism of mineralization in the Chang-

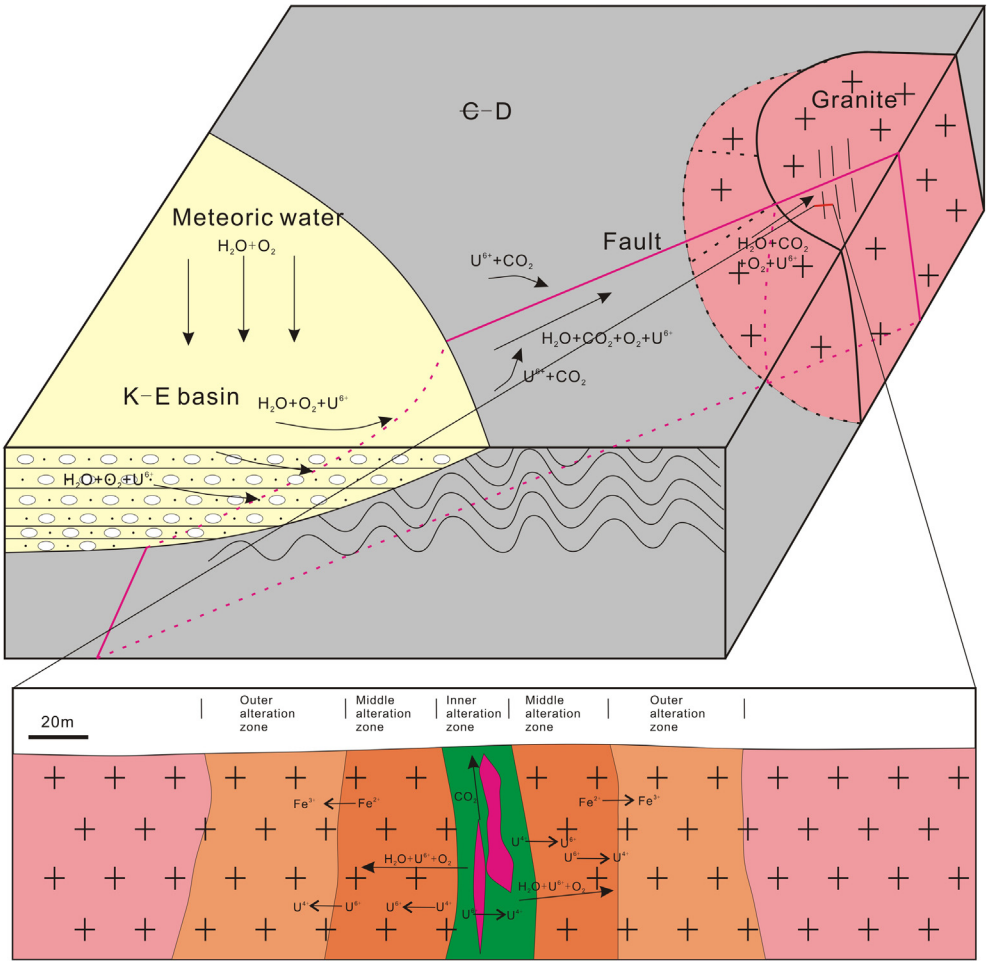

Fig. 19. Ore genesis model of the Changjiang uranium ore field.

jiang ore field involved the reduction of U^{6+} by reaction with Fe^{2+} through hydrothermal alteration, and was probably accompanied by CO_2 effervescence which would have broken apart the $UO_2(CO_3)^{2-}$ complexes.

8. Genetic model

Our studies of the fluid inclusions, H–O isotopes, and geochemistry of the Changjiang uranium ore field suggest a genetic model for the uranium mineralization that is similar to the model proposed for unconformity-related deposits (Kyser et al., 2000; Cuney et al., 2003; Cuney and Kyser, 2008). The ore-forming fluids were initially derived from meteoric water, and they became uranium- and CO_2-bearing fluids through interactions of the water with sedimentary in the Cretaceous–Paleogene basin, which made them similar to basinal fluids in terms of their H–O isotopes. The uranium-carrying fluids flowed into the Zhuguang granite massif through regional faults, and might have reacted with metamorphic basement rocks from which they extracted uranium and CO_2. When the ore-forming fluids entered the ore-bearing faults, they reacted with the granites adjacent to the faults, and this would have reduced the oxidation state, converted U^{6+} to U^{4+}, and produced a decrease in the saturated solubility of uranium. During this hydrothermal alteration, the Fe^{2+} in the granites close to the ore was converted to Fe^{3+}. In addition to this alteration, CO_2 effervescence or phase separation took place at ~250 °C and at pressures of 1000–1100 bar, leading to the release of CO_2 and the decomposition of uranyl carbonate complexes ($UO_2(CO_3)^{2-}$), thereby promoting the deposition of uranium. We propose, therefore, that this hydrothermal alteration and the CO_2 effervescence were the processes that led to the uranium mineralization in the Changjiang uranium ore field (Fig. 19). After the uranium mineralization, the Changjiang uranium ore field underwent further hydrothermal alteration under reducing conditions.

Acknowledgements

We sincerely thank Chunying Guo, Zhishuai Tang, Yaqing Pang, and Zongqiang Xia for their constructive reviews and earnest help in correcting some problems and their assistance in laboratory and fieldwork. The manuscript benefited considerably from critical reviews and helpful comments from the editor and reviewers.

Appendix

See Appendix A–C.

Appendix A
Microthermometry data.

Sample No.	Fluid inclusion No.	Fluid inclusion type	Fill	Melting TCO_2	$TmCO_2$ (clathrate)	$Th(CO_2)$	Tm(ice)	Homogenize into L or V	T_h	Homogenize into CO_2 or H_2O	Salinity (wt% NaCl equiv)
4-150-4	Group1-a	H_2O-CO_2	80	−57	7.2	29.1		L	353	CO_2	5.41
4-150-4	Group1-b	H_2O-CO_2	50	−57.4	6.9	28.6		L	316	H_2O	5.94
4-150-4	Group1-c	H_2O-CO_2	70	na	na	30		V	245	CO_2	na
4-150-4	Group1-d	CO_2	100	−61.0?		17.8?		L			0
4-150-4	Group1-e	CO_2	100	na		19.2?		L			0
4-150-4	Group1-f	H_2O-CO_2	20	−57.1	7	29.4		L	318	H_2O	5.77
4-150-4	Group1-g	H_2O-CO_2	70	−58.6	?	30		V	198?	CO_2	na
4-150-4	Group1-h	H_2O-CO_2	20	−57.3	7.5	28.9		V	291	H_2O	4.87
4-150-4	Group1-i	H_2O-CO_2	30	−57.3	7.1	28.6		L	320	H_2O	5.59
4-150-4	Group1-j	H_2O-CO_2	30	−57.7	6.6	28.9		L	220?	H_2O	6.46
ZN14	Group1-a	H_2O-CO_2	30	−56.9	6.5	24.8		L	327	H_2O	6.63
ZN14	Group1-b	H_2O-CO_2	90	−57.1	6	25.3		L	342	CO_2	7.48
ZN14	Group1-c	H_2O-CO_2	80	−57.7	6.8	28.1		V	340	CO_2	6.12
ZN14	Group1-d	H_2O-CO_2	80	−57.4	4.9	26.2		V	336	CO_2	9.24
ZN14	Group2-a	H_2O-CO_2	10	na	na	25.2		L	350	H_2O	na
ZN14	Group2-b	H_2O-CO_2	30	−57.8	7	29.2		L	323	H_2O	5.77
ZN14	Group2-c	H_2O-CO_2	20	−57.2	7.9	28.4		V	354	H_2O	4.14
ZN14	Group2-d	CO_2	100	−57.4		19.4		L			0
ZN14	Group2-e	CO_2	100	−57.5		20		L			0
ZN14	Group2-f	H_2O-CO_2	50	−56.9	7.4	26.7		L	314	H_2O	5.05
ZN14	Group2-g	H_2O-CO_2	40	−57	7.1	27.9		L	323	H_2O	5.59
ZN3	Group1-a	H_2O-CO_2	40	−56.8	6.4	27.9		L	317	H_2O	6.81
ZN3	Group1-b	H_2O-CO_2	80	−57.1	8.1	26.8		L	264	CO_2	3.76
ZN3	Group1-c	H_2O-CO_2	90	−57.1	7.9	27.2		L	299	CO_2	4.14
ZN3	Group1-d	H_2O-CO_2	20	−57.3	6.9	27.4		L	302	H_2O	5.94
ZN3	Group1-e	H_2O-CO_2	30	−57.2	7.5	27.1		L	315	H_2O	4.87
ZN3	Group1-f	H_2O-CO_2	80	−58	7.4	27.7		V	288	H_2O	5.05
ZN3	Group1-g	H_2O-CO_2	50	−57	7.7	27.4		L	311	H_2O	4.51
ZN3	Group1-h	CO_2	100	−57.9		21.4		L			0
ZN3	Group1-i	CO_2	100	−57.6		22		L			0
ZN3	Group1-j	CO_2	100	−57.6		19.3		L			0
ZN45-1	Group1-a	H_2O-CO_2	50	−58.2	5.9	29.5		L	330	H_2O	7.64
ZN45-1	Group1-b	H_2O-CO_2	70	−57.9	6.3	29.8		V	304	H_2O	6.97
ZN45-1	Group1-c	H_2O-CO_2	40	na	na	28.6		L	266	H_2O	na
ZN45-1	Group1-d	H_2O-CO_2	80	−56.9	6.9	27.5		L	248	CO_2	5.94
ZN45-1	Group1-e	H_2O-CO_2	80	na	na	27.2		L	209?	CO_2	na
ZN45-1	Group1-f	CO_2	100	−57.4		22.1		L			0
ZN45-1	Group2-a	H_2O-CO_2	30	−58	7.4	26.4		L	293	H_2O	5.05
ZN45-1	Group2-b	H_2O-CO_2	30	−57.3	7.7	27.9		L	314	H_2O	4.51
ZN45-1	Group2-c	H_2O-CO_2	70	−57.6	7.1	27.5		V	328	CO_2	5.59
ZN45-1	Group2-d	H_2O-CO_2	90	−57	7.3	27.8		L	241	CO_2	5.23
ZN45-1	Group2-e	CO_2	100	−57.5		20.3		L			0
ZN45-1	Group2-f	CO_2	100	−58		19.9		L			0
ZN45-1	Group2-g	H_2O-CO_2	20	−57	6.2	27.6		L	262	H_2O	7.14
ZN45-1	Group2-h	H_2O-CO_2	50	−57.2	6.6	26.3		L	310	H_2O	6.46
ZN45-1	Group2-i	H_2O-CO_2	50	−57.2	6.7	24.5		L	290	H_2O	6.29
ZN45-1	Group3-a	H_2O	15				−2.4	L	223	H_2O	4.01
ZN45-1	Group3-b	H_2O	15				?	L	106?	H_2O	na
ZN45-1	Group3-c	H_2O	15				−3.4	L	271	H_2O	5.55
ZN45-1	Group4-a	H_2O	15				−0.8	L	254	H_2O	1.39
ZN45-1	Group4-b	H_2O	10				−2.3	L	220	H_2O	3.85
ZN45-1	Group4-c	H_2O	15				−2.2	L	199	H_2O	3.69
ZN45-1	Group4-d	H_2O	15				−1.6	L	208	H_2O	2.72
ZN45-1	Group4-e	H_2O	15				−2.7	L	193	H_2O	4.48
ZN45-1	Group4-f	H_2O	15				−2.9	L	196	H_2O	4.79
ZN45-1	Group4-g	H_2O	15				−1.5	L	237	H_2O	2.56
ZN45-1	Group4-h	H_2O	15				−2.2	L	191	H_2O	3.69
ZN10	Group1-a	H_2O	15				−2.6	L	212	H_2O	4.32
ZN10	Group1-b	H_2O	10				−1.7	L	140	H_2O	2.89
ZN10	Group1-c	H_2O	15				−3	L	209	H_2O	4.94
15029-1	Group1-a	H_2O	15				−2.6	L	230	H_2O	4.32
15029-1	Group1-b	H_2O	15				−1.9	L	136	H_2O	3.21
15029-1	Group1-c	H_2O	15				−2.3	L	211	H_2O	3.85
15029-1	Group1-d	H_2O	15				na	L	190?	H_2O	na
15029-14	Group1-a	H_2O	10				−1.8	L	214	H_2O	3.05
15029-14	Group1-b	H_2O	5				−3.1	L	172	H_2O	5.09
10029-14	Group1-c	H_2O	10				−2.4	L	205	H_2O	4.01
10029-14	Group1-d	H_2O	10				−3.0?	L	179	H_2O	4.94
10029-14	Group1-e	H_2O	5				−2.6	L	153	H_2O	4.32
10029-14	Group1-f	H_2O	5				−2.3	L	180	H_2O	3.85

Appendix A (*continued*)

Sample No.	Fluid inclusion No.	Fluid inclusion type	Fill	Melting TCO_2	$TmCO_2$ (clathrate)	$Th(CO_2)$	Tm(ice)	Homogenize into L or V	T_h	Homogenize into CO_2 or H_2O	Salinity (wt% NaCl equiv)
10029-14	Group2-a	H_2O	10				−1.9	L	208	H_2O	3.21
10029-14	Group2-b	H_2O	5				−1.5	L	227	H_2O	2.56
10029-14	Group2-c	H_2O	5				−2.4?	L	192?	H_2O	4.01
10029-1	Group1-a	H_2O	15				−2.2	L	137	H_2O	3.69
10029-1	Group1-b	H_2O	15				−1.6	L	232	H_2O	2.72
10029-1	Group1-c	H_2O	15				−1.9	L	220	H_2O	3.21
10029-1	Group1-d	H_2O	15				−1.7	L	210?	H_2O	2.89

Syn-: fluid inclusion that captured in quartz of syn-ore stage; For H_2O-CO_2 inclusion, fill is Vol% = CO_2/(CO_2 + H_2O); for H_2O inclusion, fill is V/(V + L); Tm(ice): melting temperature (°C) of ice in H_2O fluid inclusion; Tm(CO_2): melting temperature (°C) of solid CO_2 phase in H_2O-CO_2 or CO_2 fluid inclusion; Tm(clathrate): melting temperature (°C) of clathrate in H_2O-CO_2 fluid inclusion; Th(CO_2): homogenization temperature (°C) of CO_2 phase in H_2O-CO_2 or CO_2 fluid inclusion; Th(Total): finial homogenization temperature (°C) of fluid inclusion.

Appendix B
Calculated compositional and pressure data.

Sample No.	Fluid inclusion No.	Fluid inclusion type	Bulk density	Bulk molar vol	XH2O	XCO2	XNaCl	P-T isochores (P in bars at 100 °C, 200 °C, 300 °C, 400 °C, 500 °C and Th)					
								P at Th	100 °C	200 °C	300 °C	400 °C	500 °C
4-150-4	Group1-a	H_2O-CO_2	0.75	42.972	0.457	0.535	0.008	1426.28	−225.96	489.56	1109.7	1702.86	2255.7
4-150-4	Group1-b	H_2O-CO_2	0.865	28.454	0.754	0.231	0.015	1545.66	−1255.87	147.63	1357.53	2505.07	3575.2
4-150-4	Group1-c	H_2O-CO_2	na	na	na	na	na	na	na	na	na	na	na
4-150-4	Group1-d	CO_2	0.769	55.3	0	1	0		460.01	956.43	1432.9	1889.85	2331.28
4-150-4	Group1-e	CO_2	0.784	56.16	0	1	0		439.54	917.91	1377.51	1818.39	2244.34
4-150-4	Group1-f	H_2O-CO_2	0.964	21.661	0.899	0.084	0.017	2713.93	−1971.47	339.75	2360.96	4251.54	6033.81
4-150-4	Group1-g	H_2O-CO_2	na	na	na	na	na	na	na	na	na	na	na
4-150-4	Group1-h	H_2O-CO_2	0.874	22.662	0.9	0.086	0.014	1519.03	−2288.69	−142.97	1678.62	3356.24	4926.88
4-150-4	Group1-i	H_2O-CO_2	0.933	23.458	0.86	0.124	0.016	2231.69	−1834.17	165.23	1895.67	3515.24	5034.9
4-150-4	Group1-j	H_2O-CO_2	0.936	23.449	0.859	0.123	0.018	515.99	−1761.44	165.68	1865.26	3474.1	4987.28
ZN14	Group1-a	H_2O-CO_2	0.953	23.25	0.851	0.13	0.019	2573.8	−1613.54	364.48	2117.62	3784.13	5353.69
ZN14	Group1-b	H_2O-CO_2	0.755	49.789	0.25	0.744	0.006	1413.2	143.78	712.66	1210.21	1690.94	2141.95
ZN14	Group1-c	H_2O-CO_2	0.411	65.072	0.444	0.548	0.009	645.86	−118.54	229.25	529.41	818.12	1086.89
ZN14	Group1-d	H_2O-CO_2	0.4	66.464	0.433	0.554	0.014	628.77	−98.13	240.51	526.65	809.44	1070.66
ZN14	Group2-a	H_2O-CO_2	na	na	na	na	na	na	na	na	na	na	na
ZN14	Group2-b	H_2O-CO_2	0.931	23.485	0.861	0.123	0.016	2235.57	−1834.56	141.54	1857.87	3467.52	4978.45
ZN14	Group2-c	H_2O-CO_2	0.873	22.556	0.903	0.085	0.012	2679.47	−2369.64	-126.83	1744.53	3451.96	5046.5
ZN14	Group2-d	CO_2	0.782	56.29	0	1	0		436.61	912.34	1369.46	1808	2231.68
ZN14	Group2-e	CO_2	0.776	56.58	0	1	0		428.19	896.26	1346.22	1777.92	2195.02
ZN14	Group2-f	H_2O-CO_2	0.871	28.518	0.743	0.245	0.012	1626.19	−1221.46	222.63	1456.43	2615.51	3695.12
ZN14	Group2-g	H_2O-CO_2	0.899	25.867	0.806	0.179	0.015	1903.39	−1537.04	141.1	1586.61	2946.04	4216.76
ZN3	Group1-a	H_2O-CO_2	0.905	25.832	0.804	0.178	0.018	1808.82	−1455.6	158.09	1576.11	2931.18	4200.91
ZN3	Group1-b	H_2O-CO_2	0.77	42.256	0.444	0.55	0.005	974.95	−193.88	552.34	1203.06	1817.38	2389.83
ZN3	Group1-c	H_2O-CO_2	0.733	51.005	0.257	0.739	0.003	1126.01	116.12	652.69	1130.29	1583.62	2009.91
ZN3	Group1-d	H_2O-CO_2	0.971	21.609	0.896	0.087	0.017	2516.13	−1880.42	439.68	2479.05	4392.73	6198.49
ZN3	Group1-e	H_2O-CO_2	0.935	23.405	0.859	0.128	0.014	2262.93	−1839.77	241.23	2017.7	3666.89	5211.61
ZN3	Group1-f	H_2O-CO_2	0.763	42.578	0.447	0.546	0.007	1093.63	−197.54	533.66	1169.19	1775.49	2340.98
ZN3	Group1-g	H_2O-CO_2	0.865	28.551	0.749	0.24	0.011	1554.36	−1272.93	184.84	1421.51	2574.97	3647.65
ZN3	Group1-h	CO_2	0.763	57.65	0	1	0		409.01	859.18	1292.32	1708.02	2106.69
ZN3	Group1-i	CO_2	0.758	58.09	0	1	0		400.94	843.34	1269.2	1677.97	2072.95
ZN3	Group1-j	CO_2	0.783	56.22	0	1	0		437.6	914.23	1372.19	1811.53	2235.98
ZN45-1	Group1-a	H_2O-CO_2	0.863	28.719	0.75	0.231	0.019	1629.76	−1177.5	136.72	1290.67	2409.49	3453.82
ZN45-1	Group1-b	H_2O-CO_2	0.505	48.789	0.578	0.408	0.013	605.54	−422.04	122.24	586.75	1036.14	1452.1
ZN45-1	Group1-c	H_2O-CO_2	na	na	na	na	na	na	na	na	na	na	na
ZN45-1	Group1-d	H_2O-CO_2	0.408	64.999	0.445	0.546	0.009	373.47	−121.33	227.07	527.95	816.89	1085.88
ZN45-1	Group1-e	H_2O-CO_2	na	na	na	na	na	na	na	na	na	na	na
ZN45-1	Group1-f	CO_2	0.757	58.17	0	1	0		399.37	840.25	1264.67	1672.08	2065.74
ZN45-1	Group2-a	H_2O-CO_2	0.938	23.366	0.857	0.129	0.014	1929.66	−1801	276.61	2057.62	3715.43	5269.44
ZN45-1	Group2-b	H_2O-CO_2	0.93	23.455	0.861	0.126	0.013	2200.29	−1911.18	183.47	1956.92	3594.72	5126.43
ZN45-1	Group2-c	H_2O-CO_2	0.483	49.914	0.57	0.42	0.01	703.77	−404.29	127.08	580.92	1013.39	1413.94
ZN45-1	Group2-d	H_2O-CO_2	0.727	51.383	0.259	0.737	0.004	835.06	109.47	639.86	1109.45	1557.68	1979.16
ZN45-1	Group2-e	CO_2	0.774	56.88	0	1	0		423.65	887.55	1333.58	1761.58	2175.06
ZN45-1	Group2-f	CO_2	0.777	56.62	0	1	0		430.04	899.8	1351.33	1784.55	2203.1
ZN45-1	Group2-g	H_2O-CO_2	0.978	21.584	0.893	0.086	0.021	1684.1	−1750.55	443.23	2431.94	4327.5	6122.62
ZN45-1	Group2-h	H_2O-CO_2	0.879	28.43	0.741	0.243	0.016	1597.67	−1144.99	257.72	1475.2	2639.5	3726.63
ZN45-1	Group2-i	H_2O-CO_2	0.888	28.246	0.736	0.249	0.015	1458.68	1099.79	338.07	1585.23	2776.52	3889.37
ZN45-1	Group3-a	H_2O	0.866	21.384	0.9873	0	0.0127	23.96	−1841.63	−327.4	1186.82	2701.05	4215.27
ZN45-1	Group3-b	H_2O	na	na	na	0	na	na	na	na	na	na	na
ZN45-1	Group3-c	H_2O	0.812	23.08	0.9822	0	0.0178	53.97	−2097.65	−840.68	416.26	1673.24	2930.21
ZN45-1	Group4-a	H_2O	0.799	22.779	0.9957	0	0.0043	42.19	1973.29	−666.98	639.33	1945.64	3251.95

(*continued on next page*)

Appendix B (*continued*)

Sample No.	Fluid inclusion No.	Fluid inclusion type	Bulk density	Bulk molar vol	XH2O	XCO2	XNaCl	P-T isochores (P in bars at 100 °C, 200 °C, 300 °C, 400 °C, 500 °C and Th)					
								P at Th	100 °C	200 °C	300 °C	400 °C	500 °C
ZN45-1	Group4-b	H_2O	0.869	21.293	0.9878	0	0.0122	22.66	−1816.63	−286.45	1243.72	2773.9	4304.08
ZN45-1	Group4-c	H_2O	0.895	20.665	0.9883	0	0.0117	14.89	−1622.78	28.85	1680.47	3332.1	4983.73
ZN45-1	Group4-d	H_2O	0.876	20.95	0.9915	0	0.0085	18.03	−1702.83	-112.18	1478.48	3069.14	4659.79
ZN45-1	Group4-e	H_2O	0.907	20.492	0.9857	0	0.0143	13.03	−1563.71	129.29	1822.28	3515.28	5208.27
ZN45-1	Group4-f	H_2O	0.906	20.566	0.9847	0	0.0153	13.87	−1599.31	78.64	1756.6	3434.55	5112.51
ZN45-1	Group4-g	H_2O	0.835	21.961	0.992	0	0.008	31.26	−1915.42	−497.01	921.39	2339.8	3758.2
ZN45-1	Group4-h	H_2O	0.904	20.448	0.9883	0	0.0117	12.54	−1535.5	163.19	1861.88	3560.56	5259.25
ZN10	Group1-a	H_2O	0.883	21.028	0.9863	0	0.0137	19.33	−1754.23	−173.25	1407.73	2988.7	4569.68
ZN10	Group1-b	H_2O	0.952	19.319	0.9909	0	0.0091	3.55	−794.66	1203.42	3201.5	5199.59	7197.67
ZN10	Group1-c	H_2O	0.892	20.922	0.9842	0	0.0158	18.13	−1732.78	−128.93	1474.91	3078.76	4682.6
15029-1	Group1-a	H_2O	0.86	21.604	0.9863	0	0.0137	27.24	−1895.56	−418.87	1057.82	2534.51	4011.2
15029-1	Group1-b	H_2O	0.957	19.254	0.9899	0	0.0101	3.16	−723.99	1299.62	3323.22	5346.83	7370.43
15029-1	Group1-c	H_2O	0.881	21.011	0.9878	0	0.0122	19.01	−1740.65	−157.98	1424.68	3007.35	4590.02
15029-1	Group1-d	H_2O	na	na	na	0	na	na	na	na	na	na	na
15029-14	Group1-a	H_2O	0.871	21.129	0.9904	0	0.0096	20.28	−1759.02	−200.93	1357.16	2915.25	4473.35
15029-14	Group1-b	H_2O	0.934	19.984	0.9837	0	0.0163	8.05	−1303.56	516.5	2336.56	4156.62	5976.68
10029-14	Group1-c	H_2O	0.89	20.829	0.9873	0	0.0127	16.83	−1685.95	−66.85	1552.24	3171.34	4790.43
10029-14	Group1-d	H_2O	0.926	20.143	0.9842	0	0.0158	9.5	−1396.8	381.34	2159.49	3937.63	5715.78
10029-14	Group1-e	H_2O	0.948	19.583	0.9863	0	0.0137	5.02	−1016.39	910.91	2838.22	4765.52	6692.82
10029-14	Group1-f	H_2O	0.918	20.169	0.9878	0	0.0122	9.79	−1403.66	361.04	2125.75	3890.45	5655.15
10029-14	Group2-a	H_2O	0.88	20.938	0.9899	0	0.0101	17.98	−1707.27	−112.5	1482.26	3077.03	4671.8
10029-14	Group2-b	H_2O	0.85	21.589	0.992	0	0.008	26.07	−1583.29	−376.14	1101.01	2578.17	4055.32
10029-14	Group2-c	H_2O	0.905	20.471	0.9873	0	0.0127	12.79	−1549.08	146.16	1841.39	3536.62	5231.85
10029-1	Group1-a	H_2O	0.959	19.279	0.9883	0	0.0117	3.24	−742.75	1276.9	3296.56	5316.21	7335.86
10029-1	Group1-b	H_2O	0.844	21.762	0.9915	0	0.0085	28.55	−1887.94	−438.64	1010.67	2459.98	3909.29
10029-1	Group1-c	H_2O	0.864	21.318	0.9899	0	0.0101	22.75	−1809.57	−285.28	1239.02	2763.31	4287.6
10029-1	Group1-d	H_2O	0.875	21.008	0.9909	0	0.0091	18.75	−1722.54	−142.27	1438.01	3018.28	4598.56

Syn-: fluid inclusion that captured in quartz of syn-ore stage; Th: finial homogenization temperature (°C) of fluid inclusion; XH_2O: mole fraction of H_2O; XCO_2: mole fraction of CO_2; XNaCl: mole fraction of NaCl.

Appendix C

Geochemical data for granites and ores from the Changjiang uranium ore field.

Sample No.	P16 (1)	P28 (1)	P08-2 (1)	P26 (2)	P23 (2)	MH-01 (3)	392-4 (3)	P37 (3)	P41 (4)
SiO_2	76.13	75.83	72.18	71.12	68.87	72.46	79.97	72.19	80.13
Al_2O_3	13.51	12.95	14.38	14.44	15.35	13.84	8.09	14.15	9.76
Fe_2O_3	2.32	2.8	1.45	2.29	2.15	2.11	2.79	2.43	2.38
MgO	0.47	0.54	0.38	1.14	0.6	0.76	0.65	0.31	0.8
CaO	0.47	0.31	1.45	1.13	2.86	1.09	1.6	1.22	0.58
Na_2O	0.25	0.16	0.26	0.24	0.15	0.21	0.16	0.41	0.15
K_2O	4.23	4.58	6.62	5.71	4.26	5.22	3.52	5.48	3.1
MnO	0.029	0.063	0.034	0.054	0.079	0.057	0.069	0.065	0.056
TiO_2	0.035	0.014	0.013	0.076	0.084	0.022	0.13	0.066	0.076
P_2O_5	0.013	0.013	0.012	0.017	0.021	0.013	0.037	0.017	0.018
LOI	2.35	2.6	3.01	3.62	5.38	4.06	2.62	3.49	2.61
FeO	1.65	2.3	1.2	1.6	1.65	1.75	2	2	1.6
Fe_2O_3/FeO	0.29	0.11	0.10	0.32	0.19	0.09	0.28	0.10	0.38
La	7.52	12.1	10.3	28.2	47.8	7.65	39.4	30.2	26.3
Ce	18	27.1	23.5	60.7	83.9	20.4	77.2	64.7	51.5
Pr	2.54	3.12	3.33	7.51	10.1	2.98	9.3	8.1	6.22
Nd	11.8	13.1	15.4	30.7	38.8	14.2	32.9	32.1	22.9
Sm	4.14	4.57	6.85	8.47	7.33	7.21	6.32	8.81	4.89
Eu	0.14	0.262	0.331	0.411	0.29	0.141	0.453	0.61	0.244
Gd	4.7	4.99	8.3	7.7	5.78	8.99	4.72	8.14	4.49
Tb	1.15	1.21	2.14	1.74	1.01	2.32	0.766	1.77	0.864
Dy	7.72	8.09	13.5	10.4	5.69	15.6	3.83	11.1	5.25
Ho	1.53	1.6	2.7	1.98	1.12	3.29	0.694	2.23	1.02
Er	4.71	4.96	8.1	5.96	3.41	10.2	2.11	7.11	3.09
Tm	0.829	0.917	1.33	0.981	0.591	1.76	0.379	1.23	0.532
Yb	5.03	5.74	8.45	6.19	3.85	10.7	2.38	8.39	3.46
Lu	0.811	0.881	1.15	0.937	0.639	1.53	0.376	1.29	0.526
Y	44.3	38.6	59.9	50.2	33.2	88.2	20.4	63.2	28.7
ΣREE	70.62	88.64	105.38	171.88	210.31	106.97	180.83	185.78	131.29
LREE	44.14	60.25	59.71	135.99	188.22	52.58	165.57	144.52	112.05
HREE	26.48	28.39	45.67	35.89	22.09	54.39	15.26	41.26	19.23
LREE/HREE	1.67	2.12	1.31	3.79	8.52	0.97	10.85	3.50	5.83
La_N/Yb_N	1.07	1.51	0.87	3.27	8.91	0.51	11.87	2.58	5.45

Appendix C (*continued*)

Sample No.	P16 (1)	P28 (1)	P08-2 (1)	P26 (2)	P23 (2)	MH-01 (3)	392-4 (3)	P37 (3)	P41 (4)
δEu	0.10	0.17	0.13	0.15	0.13	0.05	0.24	0.22	0.16
δCe	1.01	1.06	0.98	1.00	0.89	1.05	0.96	0.99	0.95
Th	34.7	38.7	22.3	52.2	47.7	41	51.1	47.5	30.9
U	142	162	135	323	265	123	176	416	209
U/Th	4.09	4.19	6.05	6.19	5.56	3.00	3.44	8.76	6.76
Sample No.	P11 (4)	P36 (4)	P02 (4)	P05 (4)	P40 (4)	392-70 (5)	ZK-03 (5)	P19 (6)	P21 (6)
SiO_2	77.9	74.79	77.14	76.99	78.88	73.42	83.6	73.33	76.63
Al_2O_3	11.32	14.73	11.14	11.97	9.48	12.45	8	14.57	11.94
Fe_2O_3	2.81	1.95	2.07	2.42	2.07	3.07	2.92	2.08	2.84
MgO	0.52	0.62	0.53	0.5	0.56	1.41	0.39	0.71	0.62
CaO	0.28	0.4	0.17	0.33	1.54	0.27	1.3	0.24	0.27
Na_2O	0.13	0.41	0.23	0.27	0.11	0.25	0.16	0.18	0.15
K_2O	3.94	6.53	7.39	5.27	4.29	6.19	2.97	5.89	4.86
MnO	0.067	0.036	0.03	0.042	0.077	0.057	0.057	0.045	0.054
TiO_2	0.13	0.045	0.061	0.086	0.064	0.15	0.026	0.064	0.069
P_2O_5	0.045	0.014	0.02	0.018	0.017	0.043	0.012	0.016	0.017
LOI	2.6	0.37	1.02	1.89	2.59	2.51	0.32	2.76	2.34
FeO	1.15	1.45	1	1.55	1.65	2.5	2.4	1.25	2.05
Fe_2O_3/FeO	1.33	0.23	0.96	0.45	0.14	0.12	0.11	0.55	0.27
La	19.5	18.2	7.92	24.1	21.4	33.1	83	18.8	32
Ce	75.6	42.4	29.5	51.4	43.1	64.3	162	32.4	50.9
Pr	4.51	5.24	2.29	6.58	5.5	7.51	20.7	3.77	6.2
Nd	16.7	21.8	8.8	26.1	19.8	25.7	74	15	24.3
Sm	3.31	7.09	2.6	6.48	4.75	5.11	15.8	4.28	5.78
Eu	0.368	0.447	0.264	0.37	0.34	0.516	0.755	0.362	0.362
Gd	3.1	6.89	2.38	4.95	4.2	4.3	12.7	4.15	4.91
Tb	0.651	1.65	0.544	0.916	0.815	0.792	2.32	0.983	0.939
Dy	4.09	9.92	3.36	4.61	4.92	4.26	12	6.21	5.66
Ho	0.779	2.01	0.65	0.784	0.927	0.768	2.16	1.22	1.15
Er	2.49	5.89	2.05	2.33	3.1	2.44	6.34	3.77	3.29
Tm	0.476	1.04	0.341	0.343	0.515	0.43	1.01	0.681	0.573
Yb	3.24	6.34	2.39	2.37	3.62	2.74	6.2	4.39	3.74
Lu	0.478	0.911	0.364	0.345	0.528	0.415	0.937	0.664	0.626
Y	18.4	49.4	17.5	22.7	27.2	22.4	62.5	31.9	32.1
ΣREE	135.29	129.83	63.45	131.68	113.52	152.38	399.92	96.68	140.43
LREE	119.99	95.18	51.37	115.03	94.89	136.24	356.26	74.61	119.54
HREE	15.30	34.65	12.08	16.65	18.63	16.15	43.67	22.07	20.89
LREE/HREE	7.84	2.75	4.25	6.91	5.09	8.44	8.16	3.38	5.72
La_N/Yb_N	4.32	2.06	2.38	7.29	4.24	8.67	9.60	3.07	6.14
δEu	0.35	0.19	0.32	0.19	0.23	0.33	0.16	0.26	0.20
δCe	1.90	1.05	1.68	0.98	0.95	0.96	0.93	0.89	0.83
Th	33.2	24.8	51.6	54.9	30.1	48.2	132	33.5	51.9
U	152	64.6	82.1	100	54.8	48.6	223	719	2312
U/Th	4.58	2.60	1.59	1.82	1.82	1.01	1.69	21.46	44.55
Sample No.	232-11 (6)	GP01 (6)	P10 (7)	P27 (7)	ZK-05 (7)	P33 (8)	P04 (8)	P15 (8)	ZK-02 (9)
SiO_2	78.34	76.59	74.57	75.25	76.64	73.11	75.28	70.7	70.19
Al_2O_3	9.51	7.28	12.15	11.76	10.74	13.64	12.15	15.32	14.02
Fe_2O_3	3.55	2.65	2.55	3.14	3.2	2.72	2.32	2.47	3.48
MgO	0.91	0.35	0.35	0.084	0.039	0.13	0.17	0.14	0.24
CaO	0.57	1.2	0.86	0.95	0.83	0.7	0.82	0.18	0.68
Na_2O	0.25	0.15	3.17	3.06	2.54	3.05	2.73	4.92	2.92
K_2O	4.48	2.7	4.64	5.12	5.83	5.75	5.5	5.7	7.86
MnO	0.065	0.053	0.061	0.084	0.039	0.069	0.058	0.051	0.052
TiO_2	0.19	0.023	0.13	0.1	0.047	0.1	0.089	0.081	0.12
P_2O_5	0.059	0.012	0.033	0.019	0.012	0.016	0.02	0.016	0.028
LOI	1.82	2.44	1.28	0.34	<0.10	0.65	0.72	0.31	0.32
FeO	2.75	2.2	1.7	2.4	2.4	1.95	1.65	1.7	2.6
Fe_2O_3/FeO	0.18	0.09	0.39	0.20	0.22	0.28	0.29	0.34	0.23
La	25.9	12.9	26.5	35.9	11.1	24.4	23.9	22.5	7.23
Ce	47.5	31.6	54.3	74.9	24.6	52	50.8	50.6	19.6
Pr	5.55	4.99	7	10.2	3.05	6.96	6.57	6.26	1.79
Nd	20.3	20.6	29.1	38.5	11.7	25.5	25.9	25.8	6.44
Sm	5.05	6.25	7.05	10.4	3.03	6.67	6.52	7.09	1.63
Eu	0.354	0.338	0.599	0.511	0.458	0.396	0.489	0.347	0.427
Gd	4.28	6.44	6.66	9.15	2.58	5.81	5.45	7.03	1.58
Tb	0.83	1.46	1.36	1.79	0.499	1.13	1.05	1.51	0.325
Dy	4.81	9.48	8.42	10.1	2.75	6.67	5.78	9.03	1.95
Ho	0.877	1.95	1.64	1.86	0.547	1.3	1.01	1.78	0.383
Er	2.78	6.18	4.94	5.42	1.67	3.96	3.1	5.13	1.26

(*continued on next page*)

Appendix C (*continued*)

Sample No.	232-11 (6)	GP01 (6)	P10 (7)	P27 (7)	ZK-05 (7)	P33 (8)	P04 (8)	P15 (8)	ZK-02 (9)
Tm	0.477	1.11	0.853	0.943	0.307	0.651	0.457	0.82	0.23
Yb	3.14	6.92	5.45	5.67	2.06	4.25	3.42	5.02	1.53
Lu	0.431	1.04	0.865	0.902	0.34	0.641	0.458	0.756	0.227
Y	24.4	61.1	48.9	54.9	17	30.7	28.3	43.9	11.5
ΣREE	122.28	111.26	154.74	206.25	64.69	140.34	134.90	143.67	44.60
LREE	104.65	76.68	124.55	170.41	53.94	115.93	114.18	112.60	37.12
HREE	17.63	34.58	30.19	35.84	10.75	24.41	20.73	31.08	7.49
LREE/HREE	5.94	2.22	4.13	4.76	5.02	4.75	5.51	3.62	4.96
La_N/Yb_N	5.92	1.34	3.49	4.54	3.87	4.12	5.01	3.21	3.39
δEu	0.23	0.16	0.26	0.16	0.49	0.19	0.24	0.15	0.80
δCe	0.93	0.97	0.96	0.95	1.02	0.96	0.98	1.03	1.30
Th	37.5	24.5	40.8	52.4	31.1	39.7	46.2	48.7	9.79
U	1109	53581	63.6	81.7	31.9	37.1	100	72.4	15.7
U/Th	29.57	2186.98	1.56	1.56	1.03	0.93	2.16	1.49	1.60

Sample No.	P25 (9)	P30 (9)	P34 (9)	P35 (9)	P06 (10)	P38 (10)	P39 (10)	P24 (10)	P32 (11)
SiO_2	75.49	76.11	75.42	75.67	73.79	74.81	76.64	76.27	71.87
Al_2O_3	12	11.34	12.31	12.04	13.11	11.66	11.53	11.49	12.2
Fe_2O_3	2.3	3.29	2.93	2.26	2.84	2.92	2.56	2.36	2.92
MgO	0.24	0.24	0.28	0.086	0.34	0.24	0.37	0.49	0.13
CaO	0.68	0.41	0.33	0.18	0.34	0.94	0.27	0.46	1.09
Na_2O	2.54	2.33	2.42	2.9	2.26	2.42	1.73	2.31	3.68
K_2O	5.4	5.07	5.12	5.7	6.12	4.88	5.06	4.93	4.22
MnO	0.062	0.062	0.067	0.047	0.057	0.075	0.062	0.06	0.075
TiO_2	0.076	0.068	0.099	0.048	0.085	0.09	0.084	0.072	0.11
P_2O_5	0.018	0.017	0.019	0.015	0.022	0.02	0.019	0.017	0.017
LOI	1.03	0.92	0.88	0.91	0.94	1.71	1.48	1.34	3.33
FeO	1.7	2.5	2.2	1.8	2.2	2.1	2	1.55	2.45
Fe_2O_3/FeO	0.24	0.20	0.22	0.14	0.18	0.28	0.17	0.41	0.08
La	18.5	25.8	31.6	16.4	27.2	28.2	26.9	26.8	28.6
Ce	43.7	54.7	66.6	40.9	57.6	60.4	55.8	57.8	63.7
Pr	5.28	7.1	8.33	5.24	7.47	7.38	7	7.41	7.69
Nd	21.1	28.1	31.3	23.1	28.2	27.9	26.8	29	29.5
Sm	5.34	7.93	7.62	9.01	6.83	6.97	6.6	7.74	7.55
Eu	0.331	0.392	0.388	0.351	0.511	0.477	0.456	0.406	0.343
Gd	4.21	7.79	6.43	10.5	5.46	6.24	6	6.75	6.69
Tb	0.826	1.67	1.16	2.6	0.991	1.3	1.33	1.53	1.37
Dy	4.82	10.1	6.7	16.4	5.05	7.69	8.13	9.31	7.84
Ho	0.919	2.04	1.23	3.29	0.853	1.58	1.62	1.81	1.5
Er	2.6	6.2	3.68	10.3	2.7	4.99	5.02	5.56	4.71
Tm	0.441	1.09	0.631	1.96	0.381	0.876	0.887	0.921	0.75
Yb	2.92	6.88	3.95	12.3	2.79	5.79	5.55	5.9	4.95
Lu	0.438	1.05	0.604	1.88	0.392	0.856	0.86	0.929	0.75
Y	23	59.7	32.8	112	24.2	46.3	44.8	46.2	39.5
ΣREE	111.43	160.84	170.22	154.23	146.43	160.65	152.95	161.87	165.94
LREE	94.25	124.02	145.84	95.00	127.81	131.33	123.56	129.16	137.38
HREE	17.17	36.82	24.39	59.23	18.62	29.32	29.40	32.71	28.56
LREE/HREE	5.49	3.37	5.98	1.60	6.87	4.48	4.20	3.95	4.81
La_N/Yb_N	4.54	2.69	5.74	0.96	6.99	3.49	3.48	3.26	4.14
δEu	0.21	0.15	0.16	0.11	0.25	0.22	0.22	0.17	0.14
δCe	1.07	0.97	0.98	1.07	0.97	1.00	0.97	0.99	1.03
Th	38.4	44.1	45.7	29.6	46.8	34.3	38.3	51	45.8
U	41.9	55.6	57	47.6	208	200	155	528	34.2
U/Th	1.09	1.26	1.25	1.61	4.44	5.83	4.05	10.35	0.75

Sample No.	ZK-01 (11)	P01 (12)	P07 (12)	P09 (12)	P13 (12)	P18 (12)	P20 (12)	P22 (12)	P31 (12)
SiO_2	68.6	93.62	93.29	87.44	92.59	92.2	90.1	86.8	90.05
Al_2O_3	9.64	2.6	1.67	5.14	2.01	2.97	3.16	3.94	5.23
Fe_2O_3	3.52	1.94	2.86	3.02	2.55	2.08	2.5	2.86	1.01
MgO	0.45	0.1	0.15	0.59	0.16	0.25	0.2	0.31	0.17
CaO	6.6	0.19	0.35	0.32	0.8	0.29	0.98	2.07	0.19
Na_2O	1.04	0.066	0.07	0.11	0.087	0.066	0.079	0.074	0.077
K_2O	4.04	0.86	0.26	0.97	0.37	0.31	0.97	1.18	0.97
MnO	0.18	0.025	0.14	0.05	0.053	0.027	0.047	0.12	0.017
TiO_2	0.19	0.017	0.019	0.033	0.013	0.017	0.014	0.024	0.029
P_2O_5	0.053	0.013	0.047	0.013	0.015	0.023	0.01	0.013	0.011
LOI	5.63	0.55	1.08	2.27	1.26	1.55	1.78	2.26	1.79
FeO	2.55	1.1	1.9	0.9	2	1.45	1.6	1.65	0.6
Fe_2O_3/FeO	0.27	0.65	0.39	2.24	0.16	0.32	0.45	0.62	0.57
La	51.1	1.73	10.1	13.1	8.88	34.8	20.6	29.8	6.58
Ce	101	6.58	47.5	55.4	24.1	71.5	60.1	73.9	13.3

Appendix C (*continued*)

Sample No.	ZK-01 (11)	P01 (12)	P07 (12)	P09 (12)	P13 (12)	P18 (12)	P20 (12)	P22 (12)	P31 (12)
Pr	12.6	0.656	4.24	6.36	3.18	9.82	8.13	9.51	1.57
Nd	44.5	2.56	17.5	28.2	13.5	43.2	34.9	38.4	5.92
Sm	9.77	0.97	6.47	9.29	4.97	15.2	13	10.9	1.75
Eu	0.678	0.096	0.716	0.846	0.539	1.55	1.28	0.908	0.118
Gd	8.2	1.07	7.25	11.2	7.14	21.4	14.3	11.2	1.63
Tb	1.51	0.285	2.08	2.64	2.56	6.45	4.38	2.83	0.42
Dy	8.33	1.7	14.3	17.5	22	50.7	32.4	19.7	2.86
Ho	1.56	0.388	3.03	3.85	5.42	11.8	7.21	4.06	0.595
Er	4.72	1.18	10.2	12.2	20.7	41.5	23.7	13.4	2.04
Tm	0.792	0.228	1.91	1.93	3.99	8.17	4.61	2.52	0.374
Yb	5.2	1.53	14.3	12.5	30	54.7	32.6	18.3	2.59
Lu	0.784	0.225	2.05	2.09	4.79	8.92	5.03	2.81	0.412
Y	46.9	12.1	87.1	140	167	351	164	118	16.9
ΣREE	250.74	19.20	141.65	177.11	151.77	379.71	262.24	238.24	40.16
LREE	219.65	12.59	86.53	113.20	55.17	176.07	138.01	163.42	29.24
HREE	31.10	6.61	55.12	63.91	96.60	203.64	124.23	74.82	10.92
LREE/HREE	7.06	1.91	1.57	1.77	0.57	0.86	1.11	2.18	2.68
La_N/Yb_N	7.05	0.81	0.51	0.75	0.21	0.46	0.45	1.17	1.82
δEu	0.23	0.29	0.32	0.25	0.28	0.26	0.29	0.25	0.21
δCe	0.95	1.51	1.78	1.48	1.11	0.93	1.14	1.07	0.98
Th	72.3	7.89	5.94	12.2	3.47	4.99	8.37	10.8	17.4
U	52.4	766	1942	623	2506	4995	2382	3888	252
U/Th	0.72	97.08	326.94	51.07	722.19	1001.00	284.59	360.00	14.48

Sample No.	P42 (12)	392-7 (12)	392-8 (12)	392-10 (12)	232-12 (12)	MH-02 (12)	MH-03 (12)	MH-04 (12)	GP02 (12)
SiO_2	87.81	88.53	85.47	84.1	89.85	88.08	80.28	79.49	90.65
Al_2O_3	4.81	2.19	3.55	2.34	2.59	3.9	3.12	1.58	1.73
Fe_2O_3	2.59	2.44	3.74	2.86	3.2	2.7	3.84	2.42	4.3
MgO	0.33	0.82	1.4	0.39	0.65	0.43	0.35	0.13	0.16
CaO	0.31	1.63	1.85	4.65	1.18	1.22	4.92	6.94	0.23
Na_2O	0.097	0.06	0.38	0.065	0.075	0.2	0.084	0.082	0.1
K_2O	1.72	0.17	0.45	0.73	0.67	1.02	0.3	0.3	0.39
MnO	0.089	0.13	0.13	0.12	0.057	0.053	0.08	0.1	0.025
TiO_2	0.03	0.025	0.16	0.035	0.05	0.019	0.018	0.032	0.019
P_2O_5	0.013	0.013	0.029	0.015	0.023	0.015	0.016	0.031	0.015
LOI	1.72	2.8	2.7	4.45	1.59	2.3	4.5	3.84	2.14
FeO	1.6	2.1	3.2	2.55	2.7	1.9	3.1	1.6	1.4
Fe_2O_3/FeO	0.51	0.05	0.06	0.01	0.07	0.31	0.13	0.40	1.96
La	19.5	10.8	12.3	10.5	13.8	20.5	21.3	44.7	2.73
Ce	56.8	21.6	21.5	20.6	28.2	57.4	67.4	130	8.62
Pr	9.1	2.93	2.65	2.33	3.34	7.94	9.34	21.2	1
Nd	37	11	10.2	8.42	12.8	32.7	38.6	88.1	4.02
Sm	13	2.87	2.68	1.83	2.92	11.7	14.7	37.7	1.39
Eu	1.11	0.33	0.43	0.151	0.251	0.907	1.55	3.75	0.14
Gd	12.5	2.98	2.76	1.71	2.81	14.4	18.9	41.6	1.71
Tb	3.42	0.732	0.702	0.329	0.603	3.76	5.64	13.2	0.499
Dy	21.8	4.86	4.6	2.14	3.63	24.9	40.7	94.5	3.69
Ho	4.47	1.12	1	0.441	0.688	5.5	8.61	19.6	0.807
Er	14.4	3.54	3.37	1.47	2.16	17.6	29.1	67.3	2.93
Tm	2.66	0.643	0.611	0.249	0.378	3.12	5.59	13.1	0.569
Yb	18	4.37	4.26	1.84	2.47	21	38.9	93.1	3.78
Lu	2.48	0.635	0.656	0.3	0.332	3.25	5.8	13.9	0.569
Y	124	40.6	36.1	17.7	20.9	183	230	413	25.2
ΣREE	216.24	68.41	67.72	52.31	74.38	224.68	306.13	681.75	32.45
LREE	136.51	49.53	49.76	43.83	61.31	131.15	152.89	325.45	17.90
HREE	79.73	18.88	17.96	8.48	13.07	93.53	153.24	356.30	14.55
LREE/HREE	1.71	2.62	2.77	5.17	4.69	1.40	1.00	0.91	1.23
La_N/Yb_N	0.78	1.77	2.07	4.09	4.01	0.70	0.39	0.34	0.52
δEu	0.26	0.34	0.48	0.26	0.26	0.21	0.28	0.29	0.28
δCe	1.04	0.92	0.88	0.98	0.99	1.10	1.17	1.03	1.28
Th	15.5	7.35	3.93	13.6	11.2	12.8	6.48	2.38	6.86
U	721	7829	3076	905	2830	3923	17,924	37,056	1216
U/Th	46.52	1065.17	782.70	66.54	252.68	306.48	2766.05	15,569.75	177.26

Oxides and loss-on-ignition (LOI) are in wt%; rare earth elements are in ppb; U and Th are in ppm; $Fe_2O_3/FeO = [Fe_2O_3 - (10/9) * FeO]/FeO$. (1): Unaltered two mica granite; (2): Altered two mica granite, from outer alteration zone; (3): Altered two mica granite, from middle alteration zone; (4): Altered two mica granite, from inner alteration zone; (5): Altered two mica granite, close to ore; (6): Mineralized two mica granite; (7): Unaltered biotite granite; (8): Altered biotite granite, from outer alteration zone; (9): Altered biotite granite, from middle alteration zone; (10): Altered biotite granite, from inner alteration zone; (11): Altered biotite granite, close to ore; (12): Quartz-pitchblende.

References

Angus, S., Amstrong, B., de Reuck, K.M., 1979. International Thermodynamic Tables of the Fluid State, Nitrigen. Pergamon Press, Oxford, pp. 1–125.

Bakker, R.J., Jansen, J.B.H., 1994. A mechanism for preferential H_2O leakage from fluid inclusions in quartz, based on TEM observations. Contrib. Miner. Petrol. 116, 7–20.

Bodnar, R.J., Vityk, M.O., 1994. Interpretation of microthermometric data for H_2O-NaCl fluid inclusions. In: de Vivo, B., Frezzotti, M.L. (Eds.), Fluid Inclusions in Minerals: Methods and Applications. Verginia Technology, Blacksberg, pp. 117–130.

Bonhoure, J., 2007. Mecanismes de fractionnement des terres rares dans les oxydes d'uranium naturels (Unpublished Ph.D. thesis). Institute National Polytechnique de Lorraine, Nancy, p. 227.

Chen, P.R., Liu, Y., 1990. The physicochemical conditions for metallogenesis of No. 302 uranium deposit and the source and migration direction of its hydrothermal solution. Miner. Deposita 9, 149–157 (in Chinese with English abstract).

Chen, W.F., Chen, P.R., Huang, H.Y., Ding, X., Sun, T., 2007. Chronological and geochemical studies of granite and enclave in Baimashan pluton, Hunan, South China. Sci. China Earth Sci. 50, 1606–1627 (in Chinese with English abstract).

Clayton, R.N., Mayeda, T.K., 1963. The use of bromine pentafluoride in the extraction of oxygen from oxides and silicates for isotopic analysis. Geochim. Cosmochim. Acta 27, 43–52.

Clayton, R.N., O'Neil, J.R., Mayeda, T.K., 1972. Oxygen isotope exchange between quartz and water. J. Geophys. Res. 67, 3057–3067.

Cuney, M., 2010. Evolution of uranium fractionation processes through time: driving the secular variation of uranium deposit types. Econ. Geol. 105, 553–569.

Cuney, M., Brouand, M., Cathelineau, M., Derome, D., Freiberger, R., Hecht, L., Kister, P., Lobaev, V., Lorilleux, G., Peiffert, C., Bastoul, A.M., 2003. What parameters control the high grade-large tonnage of the Proterozoic unconformity related uranium deposits? In: International Conference of Uranium Geochemistry 2003, Proceedings, Nancy, pp. 123–126.

Cuney, M., Friedrich, M., 1987. Physicochemical and crystal chemical controls on accessory mineral paragenesis in granitoids: implications for uranium metallogenesis. Bull. Mineral. 110, 235–247.

Cuney, M., Kyser, K., 2008. Recent and not-so-recent developments in uranium deposits and implications for exploration. Mineralogical Association of Canada, Short Course Series, vol. 39, pp. 23–55.

Dahlkamp, J.F., 2009. Uranium Deposits of the World. Springer-Verlag, Berlin Heidelberg, pp. 86–157.

Deng, P., Shen, W.Z., Ling, H.F., Ye, H.M., Wang, X.C., Pu, W., Tan, Z.Z., 2003. The mantle-drived fluid and uranium mineralization: a case from Xianshi uranium deposit in Xiazhuang uranium orefield. Geochimica 32, 520–528 (in Chinese with English abstract).

Deng, P., Shu, L.S., Tan, Z.Z., 2003. The Geologic setting for the formation of rich uranium ores in Zhuguang-Guidong large-scale uranium metallogenic area. Geol. Rev. 49, 486–491 (in Chinese with English abstract).

Du, L.T., 1982. The Collection of Grainte-Type Uranium Deposit Papers. Atomic Energy Press, Beijing, pp. 1–74 (in Chinese).

Du, L.T., Wang, Y.M., 1984. The unity of mineralization mechanism of granite-type, volcanic-type, carbonaceous-siliceous-pelite-type, and sandstone-type uranium deposit. Radioact. Geol. 3, 1–10 (in Chinese with English abstract).

Dubessy, J., Pagel, M., Beny, J.M., Christensen, H., Hickel, B., Kosztolanyi, C., Poty, B., 1988. Radiolysis evidenced by H_2–O_2 and H_2-bearing fluid inclusions in three uranium deposits. Geochim. Cosmochim. Acta 52, 1155–1167.

Dugdale, A.L., Hagemann, S.G., 2001. The Bronzewing lode-gold deposit, Western Australia: P-T-X evidence for fluid immiscibility caused by cyclic decompression in gold-bearing quartz veins. Chem. Geol. 173, 59–90.

Elderfield, H., Greaves, M.J., 1982. The rare earth elements in seawater. Nature 296, 214–219.

Faleiros, M.F., Campanha, C.A.G., Bello, S.M.R., Fuzikawa, K., 2007. Fault-vavle action and vein development during strike-slip faulting: an example from the Ribeira Shear Zone, Southeastern Brazil. Tectonophysics 438, 1–32.

Gao, F., Lin, J.R., Zhong, Q.L., Guo, S.Y., Pang, Y.Q., Rong, J.S., Hu, Z.H., 2011a. The wall rock alteration and its geochemical characteristics of uranium deposit No. 302. Uranium Geol. 27, 274–281 (in Chinese with English abstract).

Gao, X., Shen, W.Z., Liu, L.L., Yao, W., Zhu, B., Huang, G.L., Li, Q.Y., 2011b. Geochemical characteristics and causes of wall rock alteration in the No. 302 uranium deposit, northern Guangdong. Acta Petrol. Mineral. 30, 71–82 (in Chinese with English abstract).

Guo, G.L., Liu, X.D., Pan, J.Y., Liu, C.D., Yan, Z.B., Chen, Y.P., 2010. Study of fluid inclusion from uranium deposit No. 302 in north Guangdong. Uranium Geol. 26, 350–355 (in Chinese with English abstract).

Hall, D.L., Sterner, M.S., 1993. Preferential water loss from synthetic fluid inclusions. Contrib. Mineral. Petrol. 114, 489–500.

Han, Q.W., Ma, Z.D., Zhang, H.F., Zhang, B.R., Li, F.L., Gao, S., Bao, Z.Y., 2003. Geochemistry. Geological Publishing House, Beijing, pp. 189–202.

Hu, R.Z., Bi, X.W., Peng, J.T., Liu, Y., Zhong, H., Zhao, J.H., Jiang, G.H., 2007. Some problems concerning relationship between Mesozoic-Cenzoic lithospheric extension and uranium metallogenesis in South China. Miner. Deposits 26, 139–152 (in Chinese with English abstract).

Hu, R.Z., Bi, X.W., Su, W.C., Peng, J.T., Li, C.Y., 2004. The relationship between uranium metallogenesis and crustal extension during the Cretaceous-Tertiary in South China. Earth Sci. Front. 11, 153–160 (in Chinese with English abstract).

Hu, R.Z., Li, C.Y., Ni, S.J., Liu, L., Yu, J.S., 1993. The research on the source of CO_2 that in metallogenesis hydrothermal fluid of granite-type uranium deposite in South China. Sci. China Earth Sci. 2, 189–196 (in Chinese with English abstract).

Huang, G.L., Yin, Z.P., Ling, H.F., Deng, P., Zhu, B., Shen, W.Z., 2010. Foramtion age, geochemical characteristics and genesis of pitchblende from No. 302 uranium deposit in northern Guangdong. Miner. Deposits 29, 352–360 (in Chinese with English abstract).

Jiang, Y.H., Jiang, S.R., Ling, H.F., 2004. The mantle-drived fluid and uranium mineralization. Earth Sci. Front. 11, 491–499 (in Chinese with English abstract).

Jin, J.F., Hu, R.Z., 1987. Transportation and deposition of uranium in hydrothermal ore-forming fluids as exemplified by uranium deposit No. 302. Geochimica 4, 320–329 (in Chinese with English abstract).

Johnson, E.L., Hollister, L.S., 1995. Syndeformational fluid trapping in quartz: determining the presser-temperature conditions of deformation from fluid inclusions and the formation of pure CO_2 fluid inclusions during grain boundary migration. J. Metamorph. Geol. 13, 239–249.

Kohtaro, U., Asuka, Y., Sachihiro, T., 2008. Stretching of fluid inclusions in calcite as an indicator of frictional heating on faults. Geology 36, 111–114.

Kojima, S., Takeda, S., Kogita, S., 1994. Chemical factors controlling the solubility of uraninite and their significance in the genesis of unconformity-related uranium deposits. Miner. Deposita 29, 353–360.

Kyser, T.K., Hiatt, E., Renac, C., Durocher, K., Holk, G., Deckart, K., 2000. Diagenetic fluids in paleo-and meso-proterozoic sedimentary basins and their implications for long protracted fluid histories. In: Kyser, T.K. (Ed.), Fluid and Basin Evolution, Short Course 28. Mineralogical Association of Canada, pp. 225–262.

Kyser, T.K., O'Neil, J., 1984. Hydrogen isotope systematics of submarine basalts. Geochim. Cosmochem. Acta 48, 48–53.

Li, X.H., Li, Z.X., He, B., Li, W.X., Li, L.Q., Gao, Y.Y., Wang, X.C., 2012. The early Permian active continental margin and crustal growth of the Cathaysia Block: in situ U-Pb, Lu-Hf and O isotope analyses of detrital zircons. Chem. Geol. 328, 195–207.

Li, X.H., Qi, C.S., Liu, Y., Liang, X.R., Tu, X.L., Xie, L.W., Yang, Y.H., 2005. Petrogenesis of the Neoproterozoic bimodal volcanic rocks along the western margin of the Yangtze Block: new constraints from Hf isotopes and Fe/Mn ratios. Chin. Sci. Bull. 50, 2481–2486.

Li, X.W., Li, W.X., Wang, X.C., Li, Q.L., Liu, Y., Tang, G.Q., Gao, Y.Y., Wu, F.Y., 2010. SIMS U-Pb zircon geochronology of porphyry Cu-Au-(Mo) deposits in the Yangtze River Metallogenic Belt, Eastern China: magmatic response to early Cretaceous lithospheric extension. Lithos 119, 427–438.

Lin, X.J., 1990. The discussion on isotopic age and uranium sources of uranium deposits in Gan-Hang structure belt. Uranium Geol. 6, 257–264 (in Chinese with English abstract).

Lu, H.Z., Fan, H.R., Ni, P., Ou, G.X., Shen, K., Zhang, W.H., 2004. Fluid Inclusion. Science Press, Beijing, pp. 64–278.

Ludwig, R.K., Wallage, R.A., Simmons, R.K., 1985. The Schwartzwalder uranium deposit, II: age of uranium mineralization and lead isotopic constraints on genesis. Econ. Geol. 80, 1858–1871.

Min, M.Z., Fang, C.Q., Fayek, M., 2005. Petrography and genetic history of coffinite and uraninite from the Liueryiqi granite-hosted uranium deposit, SE China. Ore Geol. Rev. 26, 187–197.

Min, M.Z., Luo, X.Z., Du, G.S., He, B.A., Campbell, A.R., 1999. Mineralogical and geochemical constranits on the genesis of the granite-hosted Huangao uranium deposit, SE China. Ore Geol. Rev. 14, 105–127.

Neal, C., Stranger, G., 1983. Hydrogen generation from mantle source rocks in Oman. Earth Planet. Sci. Lett. 66, 1203–1225.

Nechayeva, O.L., 1968. Hydrogen in gases dissolved in water of the west Siberian Plain. Dokl. Akad. Nauk SSSR 179, 961–962.

Neumayr, P., Hagemann, S., 2002. Hydrothermal fluid evolution within the Cadillac tectonic zone, Abitibi greenstone belt, Canada: relationship to auriferous fluid in adjacent second and third-order shear zones. Econ. Geol. 97, 1203–1225.

Ni, S.J., Hu, R.Z., Jin, J.F., 1994. A vertical zoning model generated by the mixing and boiling of hydrothermal solution for uranium deposit No. 302. Uranium Geol. 10, 70–77 (in Chinese with English abstract).

Pagel, M., 1982. The mineralogy and geochemistry of uranium, thorium, and rare-earth-elements in two radioactive granites of the Vosges, France. Mineral Mag. 46, 152–163.

Parks, G.A., Pohl, D.C., 1988. Hydrothermal solubility of uraninite. Geochim. Cosmochim. Acta 52, 863–875.

Planavsky, N., Bekker, A., Rouxel, O.J., Kamber, B., Hofman, A., Knudsen, A., Lyons, T. W., 2010. Rare earth element and yttrium compositions of Archean and Paleoproterzoic Fe formations revisited: new perspectives on the significance and mechanisms of deposition. Geochim. Cosmochim. Acta 74, 6387–6405.

Ramboz, C., Pichavant, M., Weisbrod, A., 1982. Fluid immiscibility in natural processes: use and misuse of fluid inclusion data: II. Interpretation of fluid inclusion data in terms of immiscibility. Chem. Geol. 37, 29–48.

Robb, L.J., 2005. Introduction to Ore-Forming Processes. Blcakwell Publishing Company, Oxford, pp. 166–168.

Romberger, S.B., 1984. Transport and deposition of uranium in hydrothermal systems at temperatures up to 300 °C, with genetic implications. Geology of Uranium Deposits, Special Vol. 32. Canada Institute of Mining Metallogenesis, pp. 12–17.

Shepherd, T.J., Rankin, A.H., Alderton, D.H.M., 1985. A Practical Guide to Fluid Inclusion Studies. Blackie and Sons, New York, p. 232.

Sherlock, R.L., Jowett, C.E., Smith, B.D., Irish, D.E., 1993. Distinguishing barren and auriferous veins in the Sigma mine, Val-d'Or, Quebec. Can. J. Earth Sci. 30, 413–419.
Shock, E.L., Sassani, D.C., Betz, H., 1997. Uranium in geologic fluids: estimates of standard partial molal properties, oxidation potentials, and hydrolysis constants at high temperatures pressures. Geochim. Cosmochim. Acta 61, 4245–4266.
Sibson, H.R., 2001. Seismogenic framework for hydrothermal transport and ore deposition. Rev. Econ. Geol. 14, 25–50.
Sibson, H.R., 2004. Controls on maximum fluid overpressure defining conditions for mesozonal mineralisation. J. Struct. Geol. 26, 1127–1136.
Sun, T., 2006. A new map showing the distribution of the granites in South China and its explanatory notes. Geol. Bull. China 25, 332–335 (in Chinese with English abstract).
Taylor, B.E., 1987. Stable isotope geochemistry of ore-forming fluids. In: Stable Isotope Geochemistry of Low-Temperature Fluids, Short Course 13. Mineralogical Association of Canada, pp. 337–445.
Wang, L.K., Liu, T.G., 1987. The H, O, S, and Pb isotopic research on granite-type uranium deposits in South China. Geochimica 1, 67–77 (in Chinese with English abstract).
Wang, Q., Li, J.W., Jian, P., Zhao, Z.H., Xiong, X.L., Bao, Z.W., Xu, J.F., Li, C.F., Ma, J.L., 2005. Alkaline syenites in Eastern Cathaysia (South China): link to Permian-Trassic transtension. Earth Planet. Sci. Lett. 230, 339–354.
Wang, Y.J., Fan, W.M., Zhang, G.W., Zhang, Y.H., 2013a. Phanerozoic tectnoics of the South China Block: key observation and controversies. Gondwana Res. 23, 1273–1305.
Wang, Y.J., Zhang, A.M., Fan, W.M., Zhang, Y.H., Zhang, Y.Z., 2013b. Origin of paleosubduction-modified mantle for Silurian gabbro in the Cathaysia Block: geochronological and geochemical evidence. Lithos 160, 37–54.
Wang, Y.W., Ding, D.X., 2007. The study on relation between the character of wall-rock alteration and uranium-mineralization at No. 302 uranium deposit. J. Univ. South China Sci. Technol. 21, 33–36 (in Chinese with English abstract).
Wang, Z.Q., Li, Z.Y., 2007. Discussion on mantle-drived uranium mineralization. Geol. Rev. 53, 433–440 (in Chinese with English abstract).
Xavier, R.P., Foster, R.P., 1999. Fluid evolution and chemical controls in the Fazenda Maria Preta (FMP) gold deposit, Rio Itapicuru greenstone belt, Bahia, Brazil. Chem. Geol. 154, 133–154.
Zhang, B.T., 1994. The geochemical evidence for uranium mineralization and migration in granites for South China. Geochimica 23, 161–167 (in Chinese with English abstract).
Zhang, B.T., Chen, P.R., Kong, X.G., 2003. Geochemical evidence for contribution of ore-forming material to the No. 6710 uranium orefield by the Baimianshi peraluminous granite basement, Southern Jiangxi Province. Geochimica 32, 201–207 (in Chinese with English abstract).
Zhang, B.W., Deng, P., Yu, W.Y., Lu, Y.X., Zhu, B., Zhang, J.X., Cai, X.Y., 2005. Urnaium Deposit in South China. Bureau of Geology, China National Nuclear Corporation, pp. 120–264, (In Chinese).
Zhang, G.Q., 2008. Geochemistry of Hydrothermal Uranium Deposits in South China: A Case Study of the No. 302 Uranium Deposit. Chinese Academy of Science, Guiyang, pp. 1–96 (in Chinese with English abstract).
Zhang, L.G., Chen, Z.S., Liu, J.X., Yu, G.X., Wang, K.F., Wang, B.C., Xu, J.F., Zheng, W.S., Li, D.Y., Li, H., Hou, D.Y., 1995. Isotopic Exchange Theories of Two Stages During Water-Rock Reaction, and Their Applications in Exploration. Geological Press, Beijing, pp. 14–41.
Zhang, Y.C., 2002. The alkaline mantle fluid and uranium mineralization in Zhuguang, and Guidong granite. Uranium Geol. 18, 210–219.
Zhu, B., Ling, H.F., Shen, W.Z., Gao, J.F., Deng, P., Huang, G.L., Tan, Z.Z., 2006. Isotopic geochemistry of Shituling uranium deposit, Northern Guangdong Province, China. Miner. Deposits 25, 71–82 (in Chinese with English abstract).
Zinger, A.S., 1962. Molecular hydrogen in gas dissolved in waters of oil gas fields, lower Volga region. Geochem. Int. 10, 890–898.
Zoheir, B.A., El-Shazly, A.K., Helba, H., Khalil, K.I., Bodnar, R.J., 2008. Origin and evolution of the Um Egat and Dungash Orogenic gold deposits, Egyptian Eastern Desert: evidence from fluid inclusions in quartz. Econ. Geol. 103, 405–424.